Elastic and inelastic scattering of neutrinos and weakly interacting massive particles on nuclei

R. Sahu [1,*] D. K. Papoulias [2,†] V. K. B. Kota [3,‡] and T. S. Kosmas [2,§]

[1]*National Institute of Science and Technology, Palur Hills, Berhampur 761 008, Odisha, India*

[2]*Division of Theoretical Physics, University of Ioannina, GR 45110 Ioannina, Greece*

[3]*Physical Research Laboratory, Ahmedabad 380 009, India*

(Received 16 April 2020; revised 10 July 2020; accepted 18 August 2020; published 8 September 2020)

The event rates for WIMP-nucleus and neutrino-nucleus scattering processes, expected to be detected in ton-scale rare-event detectors, are investigated. We focus on nuclear isotopes that correspond to the target nuclei of current and future experiments looking for WIMP- and neutrino-nucleus events. The nuclear structure calculations, performed in the context of the deformed shell model, are based on Hartree-Fock intrinsic states with angular momentum projection and band mixing for both the elastic and the inelastic channels. Our predictions in the high-recoil-energy tail show that detectable distortions of the measured/expected signal may be interpreted through the inclusion of the nonnegligible incoherent channels.

DOI: 10.1103/PhysRevC.102.035501

I. INTRODUCTION

The recent observation of a coherent elastic neutrino nucleus scattering (CEνNS) process in the COHERENT experiment [1,2] has opened up a wide range of new opportunities to test the standard model (SM) predictions [3,4] as well as to investigate possible new physics signatures [5] (for a recent review see Ref. [6]). Being a rapidly developing field, currently there are numerous projects aiming to measure this process at the Spallation Neutron Source (SNS) [7], at the European Spallation Source (ESS) [8], or near nuclear reactors such as CONUS [9], CONNIE [10], MINER [11], TEXONO [12], RED100 [13], RICOCHET [14], and NUCLEUS [15]. Furthermore, there is an intimate connection between dark matter (DM) and neutrino experiments [16–18]. Weakly interacting massive particles (WIMPs) are probably the most promising nonbaryonic cold DM candidates [19]. The latter arise in various frameworks beyond the SM, and various experiments [20] such as DarkSide [21], DEAP-3600 [22], CDEX [23,24], SuperCDMS [25], LUX [26], XENON1T [27], DARWIN [28], and PandaX-II [29] are looking for tiny WIMP signals. The most appealing WIMP candidate is the lightest supersymmetric particle (LSP), which is expected to be stable and interacts very weakly with matter. In most cases, it is the lightest neutralino, which is a linear combination of the four neutral fermions $\tilde{B}$, $\tilde{W}_3$, $\tilde{H}_1$, and $\tilde{H}_2$, with $\tilde{B}$ and $\tilde{W}_3$ being the supersymmetric (SUSY) partners of the $U(1)$ gauge field B and the third component of the SU(2) gauge field W_3, while $\tilde{H}_1$ and $\tilde{H}_2$ are the SUSY partners of the light and heavy Higgs scalars [30].

The early data from the Cosmic Background Explorer (COBE) [31] and Supernova Cosmology project [32] implied that most of the DM is cold. Moreover, the recent WMAP [33] and Planck satellite [34] data showed that about 26.8% mass of the universe is nonluminous DM; the luminous matter forms only 4.9% of the mass, with the other 68.3% being dark energy. There are many experimental efforts to detect the elusive, yet to be observed WIMPs which interact weakly with matter. Occasionally, the latter will collide with the nuclei of the detector and the resulting recoil may provide the fingerprints regarding their existence. One such effort is the Super CDMS SNOLAB project (Sudbury, Canada) using silicon and germanium crystals. For details regarding other experimental attempts, see Refs. [26,29,35–40]. There are also efforts to search DM Axion candidates using low-noise superconducting quantum amplifiers, being hypothetical particles originally postulated to solve the strong CP problem. The Axion Dark Matter Experiment (ADMX), at the University of Washington, reported results [41] showing that "it is the world's first and only experiment to have achieved the sensitivity" to hunt for DM axions.

The odd-A isotopes ^{127}I, ^{133}Cs, and ^{133}Xe studied in this work are among the most popular nuclei, used in many experiments as detectors, for both WIMP-nucleus [42–45] and CEνNS searches [46]. It is noteworthy that the detection techniques for WIMP-nucleus scattering and CEνNS are closely related, i.e., in both cases only nuclear recoil events are required. On the other hand, a CEνNS event can perfectly mimic WIMP-nucleus scattering, thus being an irreducible background to direct detection DM searches, hence the neutrino floor is an important source of background [47–50]. This work is an extension of Ref. [5], where we have investigated the impact of new physics interactions due to neutrino magnetic moments and Z' mediators by evaluating the expected CEνNS event rates in ton-scale direct DM detection experiments. According to our findings, the latter processes could

*rankasahu@gmail.com

†d.papoulias@uoi.gr

‡vkbkota@prl.res.in

§hkosmas@uoi.gr

 ©2020 American Physical Society

potentially constitute a major source of background events. Specifically, these results indicate that the novel contributions may lead to a distortion of the expected recoil spectrum that could limit the sensitivity of direct search experiments. At the same time, given the low-threshold capabilities of the next-generation DM experiments, the observation of solar CEνNS events in a DM experiment will be a direct confirmation of its low-mass WIMP sensitivity [51]. While the potential of probing physics beyond the SM through CEνNS measurements with large-scale DM detectors has been exhaustively tested, nuclear physics inputs remain a large source of uncertainty [52]. Regarding elastic processes, the latter is encoded in the nuclear form factor, which if not properly addressed can lead to a misleading interpretation of a neutrino- or WIMP-induced signal.

In the literature there are a considerable number of theoretical calculations which describe several aspects of CEνNS and direct detection of DM through nuclear recoils. For the case of CEνNS, realistic nuclear structure calculations have been previously performed, based on various models such as the quasiparticle random phase approximation (QRPA) [53], microscopic quasiparticle phonon model (MQPM) [54], coupled-cluster theory [55], Hartree-Fock (HF) + Bardeen-Cooper-Schrieffer (BCS) calculations [56], and Hartree-Fock with a Skyrme (SkE2) nuclear potential [57]. For elastic WIMP-nucleus scattering, apart from the dominant scalar interaction, one needs to consider spin-spin interaction coming from the axial current. On the other hand, for the case of inelastic scattering, the scalar interaction practically does not contribute. The scalar interaction can arise from squark exchange, Higgs exchange, the interaction of WIMPs with gluons, etc. Some theoretical calculations are described in Refs. [58–61], while recently in Ref. [62] the authors examined the possibility of detecting electrons in light WIMP mass searches. They considered a particle model involving WIMPs interacting with electrons through the exchange of Z bosons and found that event rates of 0.5–2.5 per kg $\cdot$ yr would be possible in this scenario. Moreover, shell model calculations [63–66] have been performed to study DM event rates with ^{129,131}Xe, ^{127}I, ^{73}Ge, ^{29}Si, ^{27}Al, ^{23}Na, and ^{19}F as detectors (for heavier nuclei, a truncated shell model space is employed).

In recent years, the deformed shell model (DSM), based on HF deformed intrinsic states with angular momentum projection and band mixing, has been established for the reliable description of several nuclear properties. The model proved quite successful in the mass range $A = 60-90$ [67], in describing spectroscopic properties including spectroscopy of $N = Z$ odd-odd nuclei with isospin projection [68], in double-beta-decay half-lives [69,70], in $\mu \to e$ conversion in the field of nuclei [71], etc. Recently it was employed to study the event rates for WIMP with ^{73}Ge as the detector [37]. In addition to the energy spectra and magnetic moments, the model was used to calculate the spin structure functions, nuclear structure factors for elastic and inelastic WIMP-nucleus scattering. Furthermore, within the framework of the DSM we have recently calculated various new physics processes that could potentially contribute to CEνNS and the respective neutrino floor [5], not only for ^{73}Ge but also for other promising nuclei such as ^{71}Ga, ^{75}As, and ^{127}I.

One of the purposes of the present paper is to describe in detail the results for ^{127}I, ^{133}Cs, and ^{133}Xe and also to study the coherent and incoherent event rates for both neutrino-nucleus and WIMP-nucleus scattering. We should stress that the DSM is applied to nuclei beyond $A = 90$ for the first time in the present analysis. For neutrino-nucleus scattering, in addition to the aforementioned isotopes we have also considered the ^{23}Na, ^{40}Ar, and ^{73}Ge nuclear targets (DSM results for the spectroscopic properties of ^{23}Na and ^{40}Ar will be presented elsewhere). The paper is organized as follows: in Sec. II we summarize the most important features of the adopted nuclear DSM, while in Secs. III and IV we discuss the formalism of coherent and incoherent WIMP-nucleus and neutrino-nucleus scattering, respectively. Finally, our results are discussed in Sec. V and our main conclusions in Sec. VI.

II. DEFORMED SHELL MODEL

The details of this model have been described in our earlier publications (for details see [67]). Assuming axial symmetry for a given nucleus, starting with a model space consisting of a given set of single-particle (sp) orbitals and an effective two-body Hamiltonian (TBME + spe), the lowest-energy intrinsic states are obtained by solving the HF single-particle equation self-consistently. Excited intrinsic configurations are obtained by making particle-hole excitations over the lowest intrinsic state. It is noteworthy that these intrinsic states denoted $\chi_K(\eta)$ do not have definite angular momenta. Hence, states of good angular momentum, projected from an intrinsic state $\chi_K(\eta)$, can be written in the form

$$\left|\psi^J_{MK}(\eta)\right\rangle = \frac{2J+1}{8\pi^2\sqrt{N_{JK}}}\int d\Omega D^{J^*}_{MK}(\Omega)R(\Omega)|\chi_K(\eta)\rangle, \quad (1)$$

where N_{JK} is the normalization constant given by

$$N_{JK} = \frac{2J+1}{2}\int_0^\pi d\beta \sin\beta d^J_{KK}(\beta)\langle\chi_K(\eta)|e^{-i\beta J_y}|\chi_K(\eta)\rangle. \quad (2)$$

Here, $R(\Omega) = \exp(-i\alpha J_z)\exp(-i\beta J_y)\exp(-i\gamma J_z)$ denotes the general rotation operator and Ω represents the Euler angles (α, β, γ). The good angular momentum states projected from different intrinsic states are not in general orthogonal to each other, hence, band mixing calculations are performed after appropriate orthonormalization. The resulting eigenfunctions are of the form

$$\left|\Phi^J_M(\eta)\right\rangle = \sum_{K,\alpha} S^J_{K\eta}(\alpha)\left|\psi^J_{MK}(\alpha)\right\rangle, \quad (3)$$

with $S^J_{K\eta}(\alpha)$ being the expansion coefficients. The nuclear matrix elements occurring in the calculation of magnetic moments, elastic and inelastic spin structure functions, etc., are evaluated using the wave functions $|\Phi^J_M(\eta)\rangle$. DSM is well established to be a successful model for transitional nuclei (with $A = 60-90$) [67–69,72,73].

In order to evaluate the WIMP-nucleus scattering event rates, we first calculate the energy spectra and magnetic moments by employing the DSM wave functions and then compare our results with available experimental data [74]. A good agreement with experiment ensures the reliability

of our predictions on the event rates. In our nuclear structure calculations for ^{127}I, ^{133}Cs, and ^{133}Xe, the single-particle orbits, their energies, and the assumed effective interaction (obtained by renormalizing the CD-Bonn potential) are taken from Ref. [75]. The model space consists of the orbitals $0g_{7/2}$, $1d_{5/2}$, $1d_{3/2}$, $2s_{1/2}$, and $0h_{11/2}$ with the closed core ^{100}Sn. The single-particle energies for the five orbitals are 0.0, 0.4, 1.4, 1.3, and 1.6 MeV for protons and 0.0, 0.7, 2.1, 1.9, and 3.0 MeV for neutrons as given in Ref. [75], while we neglect the Coulomb term in our calculations. From the experimentally measured static quadrupole moment Q for the ^{127}I nucleus, the experimental negative sign of the $E2/M1$ mixing ratios for the lighter iodine isotopes, and also different theoretical analyses, Ding *et al.* [76] concluded that ^{127}I has a slightly oblate shape at least at low excitation. Hence we restrict ourselves to HF solutions with an oblate shape for this nucleus. The lowest oblate HF single-particle spectrum is shown in Fig. 1. Also, for ^{133}Cs and ^{133}Xe the lowest HF intrinsic state, which is oblate, is shown in the same figure. As described before, we obtained the lowest HF configuration by performing an axially symmetric HF calculation for each nucleus. Then various excited configurations were obtained by making particle-hole excitations over this lowest HF configuration. We have chosen a total of six, three, and four configurations for ^{127}I, ^{133}Cs, and ^{133}Xe, respectively. These choices reproduce reliably the spectroscopic properties of the above nuclear isotopes. The calculated energy levels obtained from angular momentum projection and band mixing for each nucleus are classified into collective bands on the basis of the $E2$ transition probabilities between them. As an example, the calculated energy spectrum for ^{127}I is compared with the available experimental data in Fig. 2.

For the ^{127}I isotope, four low-lying positive-parity collective bands have been identified experimentally [76] and are reasonably well described within the DSM. First, the DSM reproduces correctly the ground-state $5/2^+$ level. Second, experimentalists have suggested that the low-lying positive-parity bands in this nucleus should be associated with the proton $d_{5/2}$ and $g_{7/2}$ configurations. An analysis of the DSM wave functions shows that these collective bands originate either from the lowest HF configuration given in Fig. 1, where the odd proton is in the $k = 5/2^+$ deformed orbit, or from the first excited intrinsic state, which mainly originates from the spherical $1d_{5/2}$ and $0g_{7/2}$ orbits. Thus, using the DSM we also predict that the collective bands for this nucleus originate mainly from the $d_{5/2}$ and $g_{7/2}$ orbitals. Turning briefly to ^{133}Cs, it can be seen that the DSM calculation reproduces correctly the ground state, which is $J = 7/2^+$. In addition, a collective band built on this level has been observed for this nucleus and the calculated $K = 7/2^+$ band is found to be somewhat compressed compared to experiment. This collective band originates mainly from the lowest oblate intrinsic state. Finally, for the case of ^{133}Xe, the experimental data show that well-defined collective bands are not present in this nucleus. The DSM is found to reproduce the ground-state spin ($3/2^+$) and also the ordering of the excited levels (spin of the first excited state is $1/2^+$). In conclusion, for the above three nuclei the DSM reproduces the spin of the ground state and the first excited level correctly and the energy of the first excited level reasonably well. Note that these two levels are important for the study of the elastic and inelastic scattering processes we are undertaking.

Clearly the DSM gives results in agreement with available experimental data and very close to those obtained from full shell model calculations for physical observables such as energy spectra and $B(E2)$ and $B(M1)$ values (see, e.g., Refs. [67,68]). As is well known, $B(M1)$ values are related to the square of the off-diagonal matrix element of the $M1$ operator, whereas the magnetic moment connects diagonal matrix elements. Thus, from such applications to different nuclear systems of the DSM the confidence level acquired is high, provided that the effective interaction in the chosen model space is reasonable. In addition, through the choice of the intrinsic states of the DSM model, a satisfactory description of energy spectra for ^{127}I, ^{133}Cs, and ^{133}Xe was obtained as shown in Fig. 2.

Regarding the values of the harmonic oscillator size parameter b used for different nuclei, they have been chosen assuming the well-known formula ($b \propto A^{1/6}$) and they are listed in Table I. In our earlier work [71] in the calculation of transition matrix elements regarding $\mu \to e$ conversion in ^{72}Ge, we had taken the value $b = 1.90$ fm. The latter provided reasonably good agreement for proton and neutron form factors and coherent matrix elements compared to other calculations and also with available experimental data. The oscillator parameters for the three nuclei are taken in a similar manner. We stress that small variations of b have no essential impact on the form factors specifically for the momentum transfer of interest in our present work.

We mention that in the calculation of WIMP-nucleus event rates, the nuclear spin plays an important role, and therefore, we also calculate the nuclear magnetic moments for the isotopes in question. The calculated magnetic moments, predicted in the framework of the DSM, for ^{127}I, ^{133}Cs, and ^{133}Xe are listed in Table II and compared with the experimental data [74]. The contributions of protons and neutrons to the orbital and spin parts are also listed in this table for the reader's convenience. Focusing on ^{127}I, the magnetic moments for the levels $5/2^+$, $7/2^+$, and $3/2^+$ are experimentally known, while the DSM calculated values with bare gyromagnetic moments are off by about a factor of 2. A similar trend is also found in the case of the ^{133}Cs isotope, while for ^{133}Xe the calculated value is 50% larger than the experimental one. It should be noted, however, that shell model calculations by Coraggio *et al.* [75], using state-dependent effective charges for the $B(E2)$ values and state-dependent quenching factors for Gamow-Teller transitions GT^+, obtained a much better agreement with the experimental data. The latter implies that a similar approach with state-dependent gyromagnetic moments in our DSM calculations is expected to reproduce the experimental magnetic moments for the nuclei in question much better.

Indeed, the use of effective gyromagnetic ratios with values $g_l = 1.5$, $g_s^p = 4$, and $g_s^n = -3.0$ leads to improved gyromagnetic moments, e.g., 2.742, 2.877, and 1.613 for the $J = 5/2^+$, $7/2^+$, and $3/2^+$ states of ^{127}I, respectively. For the states $7/2^+$ and $5/2^+$ in ^{133}Cs, the new magnetic moments are 3.884 and 2.807. For ^{133}Xe, the new magnetic moment is 1.280. These

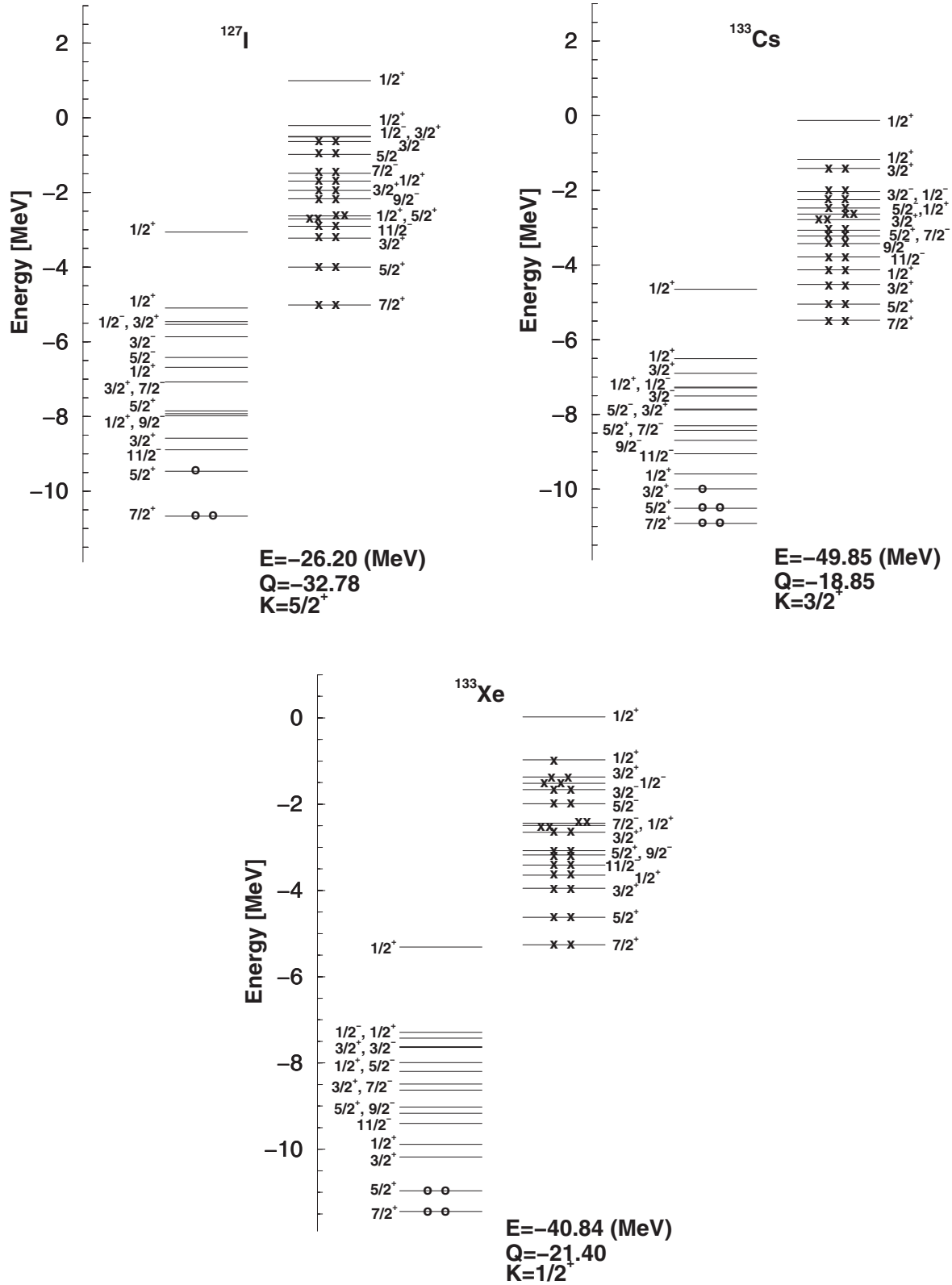

FIG. 1. HF single-particle energy spectra for ^{127}I, ^{133}Cs, and ^{133}Xe. Circles represent protons and x′s represent neutrons. The HF energy E (in MeV), mass quadrupole moment Q (in units of the square of the oscillator length parameter), and total azimuthal quantum number K are also shown.

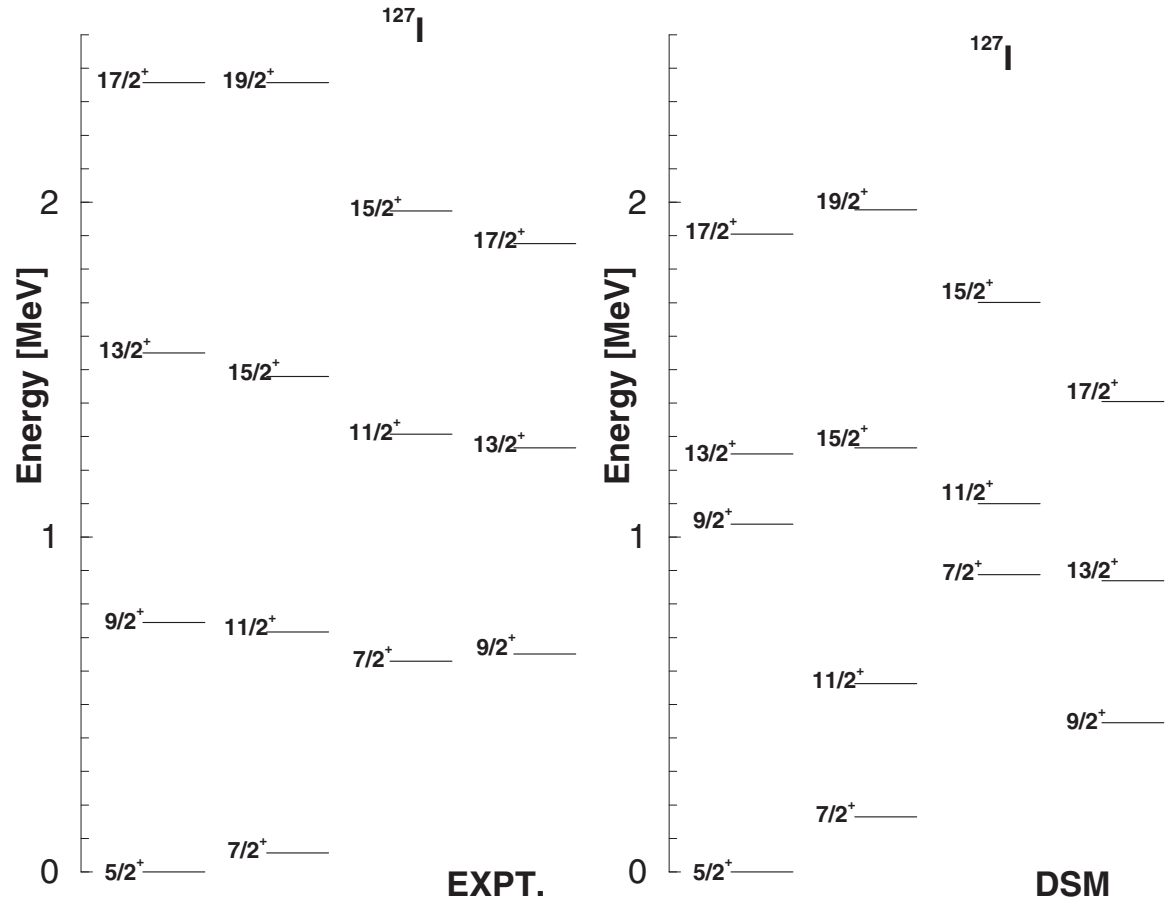

FIG. 2. Comparison of the DSM energy spectrum with the experimental data for ^{127}I. Experimental values are taken from [74].

new values of magnetic moments are in better agreement with experiment. We note that these effective gyromagnetic moments are not unique and one can obtain similar values with new sets of effective gyromagnetic ratios. Many theoretical nuclear structure calculations use effective gyromagnetic ratios in the calculation of magnetic moments. The use of effective gyromagnetic ratios does not change the nuclear wave function and hence the calculated form factors, energy spectra, etc., remain unchanged.

We furthermore note that, for ^{71}Ga, ^{73}Ge, and ^{127}I, Holmlund *et al.* [59] have calculated the magnetic moments as well as their orbital and spin parts within the MQPM and compared the obtained results with the predictions of other models. For ^{127}I, they concluded that, even though MQMP predictions were close to the single-particle estimates, the experimental values of the magnetic moments could not be exactly reproduced quantitatively. Therefore, to achieve a better reproducibility of the experimental data, detailed shell model calculations are required.

TABLE I. Values of the harmonic oscillator parameter b (in units of fm) used for different nuclei.

	Nucleus					
	^{23}Na	^{40}Ar	^{73}Ge	^{127}I	^{133}Cs	^{133}Xe
b (fm)	1.573	1.725	1.90	2.09	2.11	2.11

III. EVENT RATES FOR WIMP-NUCLEUS SCATTERING

The WIMP flux coming from the galactic halo on the Earth is expected to be quite large, of the order of 10^5 cm^{-2} s^{-1}. Even though the interaction of WIMP with matter is weak, this flux is sufficiently large for the galactic WIMPs to deposit

TABLE II. Calculated DSM magnetic moments for the different nuclear states of ^{127}I, ^{133}Cs, and ^{133}Xe. Results refer to the bare gyromagnetic ratios and are compared with the experimental ones from Ref. [74].

Nucleus	J	$\langle l_p \rangle$	$\langle S_p \rangle$	$\langle l_n \rangle$	$\langle S_n \rangle$	μ (nm)	Expt.
^{127}I	$5/2^+$	2.395	−0.211	0.313	0.002	1.207	2.813
	$7/2^+$	2.580	−0.243	1.097	0.007	0.969	2.54
	$3/2^+$	1.542	−0.181	0.148	−0.008	0.560	0.97
^{133}Cs	$7/2^+$	3.40	−0.34	0.49	−0.048	1.69	2.582
	$5/2^+$	2.47	−0.25	0.30	−0.034	1.23	3.45
^{133}Xe	$3/2^+$	0.39	−0.04	1.44	−0.285	1.26	0.81
	$1/2^+$	0.30	−0.03	0.004	0.230	−0.75	

a measurable amount of energy in an appreciably sensitive detector apparatus when they scatter off nuclei. Most of the experimental searches of WIMPs are based on the direct detection through their interaction with target nuclei. The relevant formalism of WIMP-nucleus scattering has been discussed in our earlier works [5,37] (see also Refs. [19,59,60]). For completeness, however, below we summarize briefly the most important steps. Here, we consider the spin-spin interaction and the scalar interaction. In the case of the former, the WIMP couples to the spin of the nucleus, while the scalar interaction is proportional to the square of the mass number A. In the expressions for the event rates, the particle physics (SUSY) part is separated from the nuclear part so that the role played by the nuclear physics part becomes apparent.

A. WIMP-nucleus elastic scattering

The differential event rate per unit detector mass for a WIMP with mass m_χ can be written as [20]

$$dR = N_t\ \phi\ f\ \frac{d\sigma}{d|q|^2} d^3v\ d|q|^2, \tag{4}$$

where $\phi = \rho_0 v/m_\chi$ is the DM flux, with ρ_0 being the local WIMP density, N_t stands for the number of target nuclei per unit mass, and f denotes the WIMP velocity distribution, which is assumed to be of the Maxwell-Boltzmann type. The latter takes into account the distribution of the WIMP velocity relative to the detector (or Earth) and also the motion of the Sun and Earth. Note that when the rotation of Earth around its own axis is neglected, then $v = |\mathbf{v}|$ corresponds to the relative velocity of the WIMP with respect to the detector. Finally, $q \equiv |\mathbf{q}|$ represents the magnitude of the 3-momentum transfer to the nuclear target, which is related to the dimensionless variable $u = q^2b^2/2$, with b denoting the harmonic oscillator length parameter.

The WIMP-nucleus differential cross section in the laboratory frame is then given by [19,37,59–61]

$$\frac{d\sigma(u,v)}{du} = \frac{1}{2}\sigma_0 \left(\frac{1}{m_p b}\right)^2 \frac{c^2}{v^2} \frac{d\sigma_A(u)}{du}, \tag{5}$$

with

$$\begin{aligned}\frac{d\sigma_A(u)}{du} &= \left(f_A^0\right)^2 F_{00}(u) + 2f_A^0 f_A^1 F_{01}(u) + \left(f_A^1\right)^2 F_{11}(u) \\ &+ \left[Z\left(f_S^0 + f_S^1\right)\right]^2 |F_Z(u)|^2 \\ &+ \left[(A-Z)\left(f_S^0 - f_S^1\right)\right]^2 |F_N(u)|^2 \\ &+ 2Z(A-Z)\left[\left(f_S^0\right)^2 - \left(f_S^1\right)^2\right] |F_Z(u)||F_N(u)|, \end{aligned} \tag{6}$$

where $F_Z(u)$ and $F_N(u)$ denote the nuclear form factors for protons and neutrons, respectively. In the latter expression, the first three terms correspond to the spin contribution, coming from the axial current, and the last three terms account for the coherent part, coming mainly from the scalar interaction. Here, f_A^0 and f_A^1 represent isoscalar and isovector parts of the axial vector current, and similarly f_S^0 and f_S^1 represent isoscalar and isovector parts of the scalar current. The nucleonic current parameters f_A^0 and f_A^1 depend on the specific SUSY model assumed in this work for the WIMP (lightest supersymmetric particle). However, f_S^0 and f_S^1 depend on the hadron model used to embed quarks and gluons into nucleons [77].

The normalized spin structure functions $F_{\rho\rho'}(u)$ with $\rho, \rho' = 0, 1$ in Eq. (6) are defined as

$$F_{\rho\rho'}(u) = \sum_{\lambda,\kappa} \frac{\Omega_\rho^{(\lambda,\kappa)}(u)\Omega_{\rho'}^{(\lambda,\kappa)}(u)}{\Omega_\rho \Omega_{\rho'}}, \tag{7}$$

$$\begin{aligned}\Omega_\rho^{(\lambda,\kappa)}(u) &= \sqrt{\frac{4\pi}{2J_i+1}} \times \langle J_f \| \sum_{j=1}^{A} [Y_\lambda(\Omega_j) \otimes \sigma(j)]_\kappa \\ &\times j_\lambda(\sqrt{u}\, r_j)\omega_\rho(j) \| J_i \rangle, \end{aligned} \tag{8}$$

where $\omega_0(j) = 1$ and $\omega_1(j) = \tau(j)$, with $\tau = +1$ for protons and $\tau = -1$ for neutrons, j_λ is the spherical Bessel function, and the static spin matrix elements are defined as $\Omega_\rho(0) = \Omega_\rho^{(0,1)}(0)$. The reduced matrix element appearing in Eq. (8) is then evaluated within the framework of the DSM. For this purpose, we need the sp matrix elements of the operator of the form $t_v^{(l,s)J}$, given by

$$\begin{aligned}&\langle n_i l_i j_i \| \hat{t}^{(l,s)J} \| n_k l_k j_k \rangle \\ &= \sqrt{(2j_k+1)(2j_i+1)(2J+1)(s+1)(s+2)} \\ &\times \begin{Bmatrix} l_i & 1/2 & j_i \\ l_k & 1/2 & j_k \\ l & s & J \end{Bmatrix} \langle l_i \| \sqrt{4\pi} Y^l \| l_k \rangle\ \langle n_i l_i | j_l(kr) | n_k l_k \rangle, \end{aligned} \tag{9}$$

where $\{\cdot\}$ denotes the 9-j symbol. Assuming that the polar axis is aligned along the direction of $\mathbf{v}_1$ (velocity of the Earth with respect to the Sun) and converting the integration variables into dimensionless form, the event rate is obtained by integrating Eq. (4) with respect to u, the velocity v, and the scattering angle θ, as [37]

$$\langle R \rangle_{\rm el} = \int_{-1}^{1} d\xi \int_{\psi_{\min}}^{\psi_{\max}} d\psi \int_{u_{\min}}^{u_{\max}} G(\psi,\xi) \frac{d\sigma_A(u)}{du} du. \tag{10}$$

In the above expression, $G(\psi,\xi)$ is given by

$$G(\psi,\xi) = \frac{\rho_0}{m_\chi} \frac{\sigma_0}{A m_p} \left(\frac{1}{m_p b}\right)^2 \frac{c^2}{\sqrt{\pi} v_0} \psi e^{-\lambda^2} e^{-\psi^2} e^{-2\lambda\psi\xi}, \tag{11}$$

with $\psi = v/v_0$, $\lambda = v_E/v_0$, $\xi = \cos(\theta)$. For our calculation we employed the following parameters: WIMP density $\rho_0 = 0.3$ GeV/cm^3, $\sigma_0 = 0.77 \times 10^{-38}$ cm^2, and proton mass $m_p = 1.67 \times 10^{-27}$ kg. The velocity of the Sun with respect to the galactic center is taken to be $v_0 = 220$ km/s and the velocity of the Earth relative to the Sun is taken as $v_1 = 30$ km/s. The velocity of the Earth with respect to the galactic center v_E is given by $v_E = \sqrt{v_0^2 + v_1^2 + 2v_0 v_1 \sin(\gamma)\cos(\alpha)}$, where α is the modulation angle, which stands for the phase of the Earth on its orbit around the Sun, and γ is the angle between the normal to the ecliptic and the galactic equator [30], which is taken to be $\simeq 29.8^\circ$.

For simplicity, by writing $X(1) = F_{00}(u)$, $X(2) = F_{01}(u)$, $X(3) = F_{11}(u)$, $X(4) = |F_Z(u)|^2$, $X(5) = |F_N(u)|^2$, $X(6) = |F_Z(u)||F_N(u)|$, the event rate per unit mass of the detector of

Eq. (10) can be cast in the form

$$\langle R\rangle_{\rm el} = \left(f_1^0\right)^2 D_1 + 2f_A^0 f_A^1 D_2 + \left(f_A^1\right)^2 D_3 + \left[Z\left(f_S^0 + f_S^1\right)\right]^2 D_4 + \left[(A-Z)\left(f_S^0 - f_S^1\right)\right]^2 D_5 + 2Z(A-Z)\left[\left(f_S^0\right)^2 - \left(f_S^1\right)^2\right] D_6, \quad (12)$$

where D_i is the three-dimensional integrations of Eq. (10), defined as

$$D_i = \int_{-1}^{1} d\xi \int_{\psi_{\rm min}}^{\psi_{\rm max}} d\psi \int_{u_{\rm min}}^{u_{\rm max}} G(\psi,\xi) X(i)\, du, \quad i = 1,\ldots,6. \quad (13)$$

The lower and upper limits of integrations given in Eqs. (10) and (13) are taken from Ref. [61] and read

$$\psi_{\rm min} = \frac{c}{v_0}\left(\frac{A m_p T_{\rm thres}}{2\mu_r^2}\right)^{1/2},$$

$$\psi_{\rm max} = -\lambda\xi + \sqrt{\lambda^2\xi^2 + \frac{v_{\rm esc}^2}{v_0^2} - 1 - \frac{v_1^2}{v_0^2} - \frac{2v_1}{v_0}\sin(\gamma)\cos(\alpha)},$$

$$u_{\rm min} = A m_p T_{\rm thres} b^2,$$

$$u_{\rm max} = 2(\psi\mu_r b v_0/c)^2. \quad (14)$$

Assuming the escape velocity from our galaxy to be $v_{\rm esc} = 625$ km/s, the quantity $v_{\rm esc}^2/v_0^2 - 1 - v_1^2/v_0^2$ appearing in the definition of $\psi_{\rm max}$ is equal to 7.0525, and similarly $(2v_1/v_0)\sin(\gamma) = 0.135$, while $T_{\rm thres}$ denotes the detector threshold energy and μ_r is the reduced mass of the WIMP-nucleus system.

B. WIMP-nucleus inelastic scattering

In the case of inelastic WIMP-nucleus scattering, the initial and final nuclear states do not coincide and the corresponding cross section due to the scalar current is considerably smaller with respect to the elastic case. We then focus on the spin-dependent scattering and the inelastic event rate per unit mass of the detector can be written as

$$\langle R\rangle_{\rm inel} = \left(f_1^0\right)^2 E_1 + 2f_A^0 f_A^1 E_2 + \left(f_A^1\right)^2 E_3, \quad (15)$$

where E_1, E_2, and E_3 are the three-dimensional integrals

$$E_i = \int_{-1}^{1} d\xi \int_{\psi_{\rm min}}^{\psi_{\rm max}} d\psi \int_{u_{\rm min}}^{u_{\rm max}} G(\psi,\xi) X(i)\, du. \quad (16)$$

The integration limits in the latter expression read [60,61]

$$u_{\rm min} = \frac{1}{2} b^2 \mu_r^2 \frac{v_0^2}{c^2}\psi^2\left[1 - \sqrt{1 - \frac{\Gamma}{\psi^2}}\right]^2, \quad (17)$$

$$u_{\rm max} = \frac{1}{2} b^2 \mu_r^2 \frac{v_0^2}{c^2}\psi^2\left[1 + \sqrt{1 - \frac{\Gamma}{\psi^2}}\right]^2, \quad (18)$$

where

$$\Gamma = \frac{2E^*}{\mu_r c^2}\frac{c^2}{v_0^2}, \quad (19)$$

with E^* being the energy of the excited nuclear state. Here, $\psi_{\rm max}$ is the same as in the elastic case and the lower limit $\psi_{\rm min} = \sqrt{\Gamma}$. The rest of the parameters, e.g., ρ_0, σ_0, etc., take the same values as in the elastic case.

IV. NEUTRINO-NUCLEUS SCATTERING

In this section we consider neutrino-nucleus scattering focusing on both coherent (g.s. → g.s. transitions) and incoherent channels (g.s. → excited-state transitions). In the low-energy regime of SM electroweak interactions, the latter can be well studied through an effective Lagrangian written in the approximation of four-fermion contact interaction and normalized to the Fermi coupling constant G_F, as

$$\mathcal{L}(x) = \frac{G_F}{\sqrt{2}} L_\mu(x) H^\mu(x), \quad (20)$$

where the corresponding leptonic and hadronic currents are given through the expressions

$$L_\mu(x) = \overline{\nu}(x)\gamma_\mu(1-\gamma_5)\nu(x),$$
$$H^\mu(x) = \sum_{f=n,p} \overline{\psi}_f(x)\gamma^\mu\left(g_V^f - g_A^f\gamma_5\right)\psi_f(x). \quad (21)$$

The left- and right-handed couplings are written in terms of the usual vector (axial-vector) g_V^f (g_A^f) couplings as functions of the weak mixing angle $\sin^2\theta_W \equiv s_W^2 = 0.2386$,

$$g_L^f = \tfrac{1}{2}\left(g_V^f + g_A^f\right), \quad g_R^f = \tfrac{1}{2}\left(g_V^f - g_A^f\right), \quad (22)$$

where the fundamental SM couplings of the nucleon $f = \{n, p\}$ to the Z_0 boson read

$$g_V^p = \tfrac{1}{2} - 2s_W^2, \quad g_A^p = \tfrac{1}{2},$$
$$g_L^p = \tfrac{1}{2}\left(1 - 2s_W^2\right), \quad g_R^p = -s_W^2,$$
$$g_V^n = -\tfrac{1}{2}, \quad g_A^n = -\tfrac{1}{2},$$
$$g_L^n = -1, \quad g_R^n = 0. \quad (23)$$

In what follows, the neutrino-nucleus cross sections and the corresponding event rates rely on the formalism of Bednyakov and Naumov (BN) [3], while the nuclear physics effects are incorporated by employing the DSM formalism described in Sec. II. A key difference with respect to Ref. [3] is that the DSM method adopted here predicts the excitation energies of the nuclei in question, in contrast to the BN study, where the latter are put by hand. We furthermore provide differential and integrated event rates expected in various nuclear targets for different neutrino sources.

To set up the notation, we provide below the most important features of the BN formalism. We start by denoting the 4-momentum of incoming and outgoing neutrinos as $k = (E_\nu, \mathbf{k})$ and $k' = (E'_\nu, \mathbf{k}')$, respectively, and the 4-momentum of the initial (final) nuclear state as P_n (P'_m). Then the energy of the outgoing neutrino is written in terms of the incident neutrino energy, the scattering angle θ between $\mathbf{k}$ and $\mathbf{k}'$, the nuclear excitation energy $\Delta\varepsilon_{mn}$ (i.e., the energy difference between the initial and the final nuclear states), and the nuclear mass m_A as [3]

$$E'_\nu = \frac{m_A(E_\nu - \Delta\varepsilon_{mn}) - E_\nu\Delta\varepsilon_{mn} + \Delta\varepsilon_{mn}^2/2}{m_A + E_\nu(1-\cos\theta) - \Delta\varepsilon_{mn}}, \quad (24)$$

while the energy of the recoiling nucleus reads

$$T_A = \sqrt{m_A^2 + \mathbf{q}^2} - m_A, \tag{25}$$

where $\mathbf{q}$ is the 3-momentum transfer with magnitude

$$q \equiv |\mathbf{q}| = \left(E_\nu^2 + E_\nu'^2 - 2E_\nu E_\nu' \cos\theta\right)^{1/2} \simeq (2m_A T_A)^{1/2}. \tag{26}$$

Finally, it is noteworthy that the nuclear recoil energy given in Eq. (25) can be adequately approximated by keeping only the first term in the $1/m_A$ expansion, as

$$T_A \approx \frac{E_\nu(E_\nu - \Delta\varepsilon_{mn})(1-\cos\theta) + \Delta\varepsilon_{mn}^2/2}{m_A}. \tag{27}$$

The differential coherent elastic neutrino-nucleus scattering (CEνNS) cross section in the BN formalism has been written as [3]

$$\frac{d\sigma_{\rm coh}}{dT_A} = \frac{4G_F^2 m_A}{\pi}(1-a)\left|\sum_{f=n,p}\sqrt{g_{\rm coh}^f}F_f\left(A_+^f[g_L^f - g_R^f ab(1-b)] + A_-^f g_R^f[1-ab(1-b)]\right)\right|^2, \tag{28}$$

while the corresponding differential incoherent neutrino-nucleus scattering (IνNS) cross section reads [3]

$$\frac{d\sigma_{\rm inc}}{dT_A} = \frac{4G_F^2 m_A}{\pi}\sum_{f=n,p} g_{\rm inc}^f(1-|F_f|^2)\left[A_+^f\left((g_{L,f} - g_{R,f}ab^2)^2 + g_{R,f}^2 ab^2(1-a)\right) + A_-^f g_{R,f}^2(1-a)(1-a+ab^2)\right]. \tag{29}$$

In the latter two expressions the parameters a and b are defined as

$$a = \frac{q^2}{q_{\rm min}^2} \simeq \frac{T_A}{T_A^{\rm max}}, \quad b^2 = \frac{m_f^2}{s}. \tag{30}$$

Here, $A_\pm^p \equiv Z_\pm$ ($A_\pm^n \equiv N_\pm$) represents the number of protons (neutrons) with spin $\pm 1/2$ and $s = (p+k)^2$ is the total energy squared in the center-of-mass frame (p denotes an effective 4-momentum of the nucleon). The correction factors $g_{\rm coh}^f$ and $g_{\rm inc}^f$ for coherent and incoherent processes, respectively, are of the order of unity and become more important for very low incoming neutrino energy (see the Appendix in Ref. [3]). We have furthermore verified that for CEνNS the impact of $g_{\rm coh}^f$ is less important, while for the IνNS channel the corresponding corrections due to $g_{\rm inc}^f$ become more significant. Finally, it is interesting to recall that in the case of zero momentum transfer $F_f(q=0) = 1$ holds, and therefore, the incoherent cross section vanishes due to its dependence on the quantity $1 - F_f(q)$.

V. RESULTS AND DISCUSSION

The performed nuclear structure calculations refer to the nuclear matrix elements for g.s. $\rightarrow$ g.s. transitions (elastic channel) and for transition matrix elements in the case of inelastic scattering, for both neutrino-nucleus and WIMP-nucleus processes. For the elastic and inelastic WIMP-nucleus event rates given in Eqs. (12) and (15), the nucleonic current part has been separated from the nuclear part. We note that D_i and E_i depend on the nuclear structure parameters as well as on the kinematics, assumptions regarding the WIMP velocity, and modulation effect, while $X(i)$ depend on the spin structure functions and the nuclear form factors. Thus, the nuclear structure calculations are needed for the evaluation of $X(i)$.

A. Results for WIMP-nucleus scattering

In Ref. [4] we have shown that the DSM reproduces better the experimental data from the COHERENT experiment (SNS neutrinos) compared to the widely used approximated methods like the Helm, symmetrized Fermi, and Klein-Nystrand form factors. Similarly, in Ref. [5], focusing on astrophysical neutrinos in direct detection dark-matter experiments, we showed that for a large momentum (mainly for diffuse supernova neutrino background; DSNB and atmospheric neutrinos) the difference in the event rates for DSM vs Helm can be of one order of magnitude. This work is an extension of Refs. [4,5], since here the inelastic channels are also considered. Compared to other relevant nuclear structure methods the DSM presents the advantage that it is applicable for odd-A deformed nuclear isotopes. Finally, nuclear uncertainties in such experiments are usually taken to be 10% in a statistical analysis, however, this issue is beyond the scope of our work.

In our calculations, we first evaluate the static spin matrix elements Ω_0 and Ω_1 in Eq. (8) for both elastic and inelastic scattering (see Table III). For the ground state of ^{127}I these values are -0.494 and -0.505, while for ^{133}Cs they are -0.878 and -0.660, and similarly, for ^{133}Xe the corresponding quantities are -0.835 and 0.636. Compared with other works, in Ref. [60] the authors, using effective g factors, evaluated the elastic and inelastic event rates for ^{127}I and found that for elastic scattering the values of Ω_0^2 and Ω_1^2 are 0.350 and 0.226,

TABLE III. Calculated static spin matrix elements Ω_0 and Ω_1 for elastic and inelastic channels.

	Elastic		Inelastic	
Nucleus	Ω_0	Ω_1	Ω_0	Ω_1
^{127}I	-0.494	-0.505	-0.276	0.019
^{133}Cs	-0.878	-0.660	0.020	0.041
^{133}Xe	-0.835	0.636	-0.031	0.013

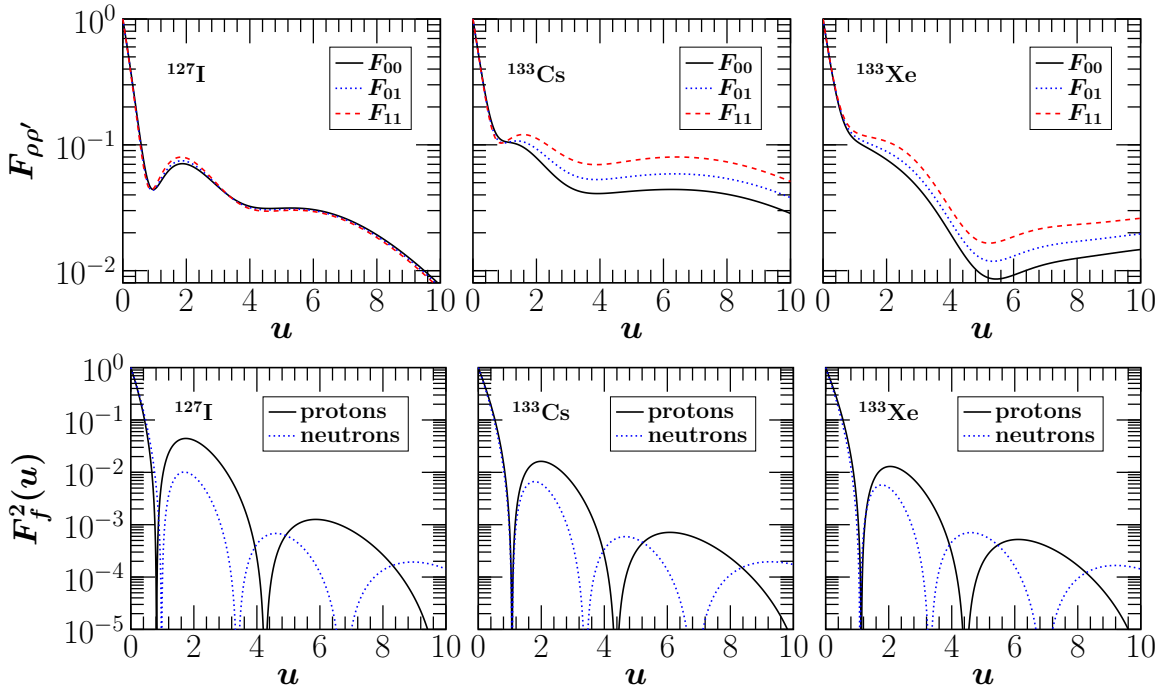

FIG. 3. Normalized spin structure functions (upper panels) and squared proton and neutron nuclear form factors (lower panels) for the ground state of the ^{127}I, ^{133}Cs, and ^{133}Xe isotopes.

i.e., of the same order of magnitude as in our case. They also found that Ω_0 and Ω_1 have the same sign. The DSM wave functions given by Eq. (3) are used to calculate the normalized spin structure functions $F_{\rho\rho'}(u)$ and the squared nuclear form factors $|F_{Z,N}(u)|^2$ for the chosen set of nuclei. The results are shown in Fig. 3 as a function of u. As can be seen, for the case of ^{127}I, the structure functions F_{00}, F_{01}, and F_{11} show little variation up to about $u = 10$. However, for ^{133}Cs the spin structure functions show variations from each other above $u = 1$ (a similar trend was found in Ref. [60]). Also, the DSM results for ^{133}Xe show a similar trend. The proton and neutron nuclear form factors for ^{127}I have the same values up to about $u = 0.8$, while beyond this value the minima of the neutron form factors are shifted towards smaller u in comparison to those of protons. The form factors for ^{133}Cs and ^{133}Xe show a similar trend as in ^{127}I.

In Fig. 4, the nuclear-structure-dependent coefficients D_i, $i = 1, \ldots, 6$, given in Eqs. (13) are plotted for ^{127}I, ^{133}Cs, and ^{133}Xe, respectively, as functions of the WIMP mass m_χ for different values of the detector threshold. The peaks of these nuclear structure coefficients occur at around $m_\chi \approx 30$ GeV in the case of zero threshold energy and they shift towards higher values of m_χ upon going to higher threshold energies. In this work, we studied also the crucial annual modulation effect [43], which is expected to provide strong evidence regarding the observation of DM since the background does not exhibit such modulation. In Fig. 4 this effect is represented by the thickness of the graphs and it is pronounced near the peaks. For ^{127}I, our present results have been obtained assuming threshold energies $T_{\text{thres}} = 0$, 10, and 20 keV, in good agreement with Ref. [60]. It can be seen that the annual modulation effect is much smaller for this detector nucleus, while a similar trend is seen for the other two nuclei. On the other hand, in the case of ^{133}Cs the values of D_i are larger (by a factor of more than 2) compared to those for ^{127}I, while in the case of ^{133}Xe, D_i have values similar to those for ^{133}Cs but D_2 is negative. Finally, the contributions to the rate driven by the coefficients D_4, D_5, and D_6, i.e., due to proton, neutron, and overlap of proton and neutron form factors, respectively, are similar for all nuclei.

The detection event rates for the studied nuclei have been calculated at a particular WIMP mass by reading out the corresponding values of D_i in Fig. 4 for each nucleus and by using Eq. (10) assuming the nucleonic current parameters $f_A^0 = 3.55 \times 10^{-2}$, $f_A^1 = 5.31 \times 10^{-2}$, $f_S^0 = 8.02 \times 10^{-6}$, and $f_S^1 = -0.15 \times f_S^0$. Figure 5 illustrates the present results as a function of the WIMP mass m_χ for ^{127}I, ^{133}Cs, and ^{133}Xe. The following conclusions can be drawn: for $T_{\text{thres}} = 0$ keV, the highest event rate occurs for ^{127}I at $m_\chi \sim 35$ GeV, while for ^{133}Cs and ^{133}Xe, the highest event rates occur at $m_\chi = 40$ GeV. The event rate decreases at a higher detector threshold energy but the peak shifts to higher values of m_χ.

We now turn our attention to the inelastic channels of WIMP-nucleus scattering. For ^{127}I, the first excited state $7/2^+$ appears at 57.6 keV above the ground state. It is thus interesting to note that exotic WIMPS can potentially lead to large nucleon spin-induced cross sections, which in turn can lead to a relatively high probability for inelastic WIMP-^{127}I scattering. The latter emphasizes the significance of our present results for inelastic scattering and motivates further study. The static spin matrix elements Ω_0 and Ω_1 have values of -0.276 and 0.019, respectively. Note that unlike the elastic case, Ω_0 and Ω_1 have opposite signs. Again, the magnitude of Ω_0 is smaller by a factor of 2 compared to the elastic case, whereas

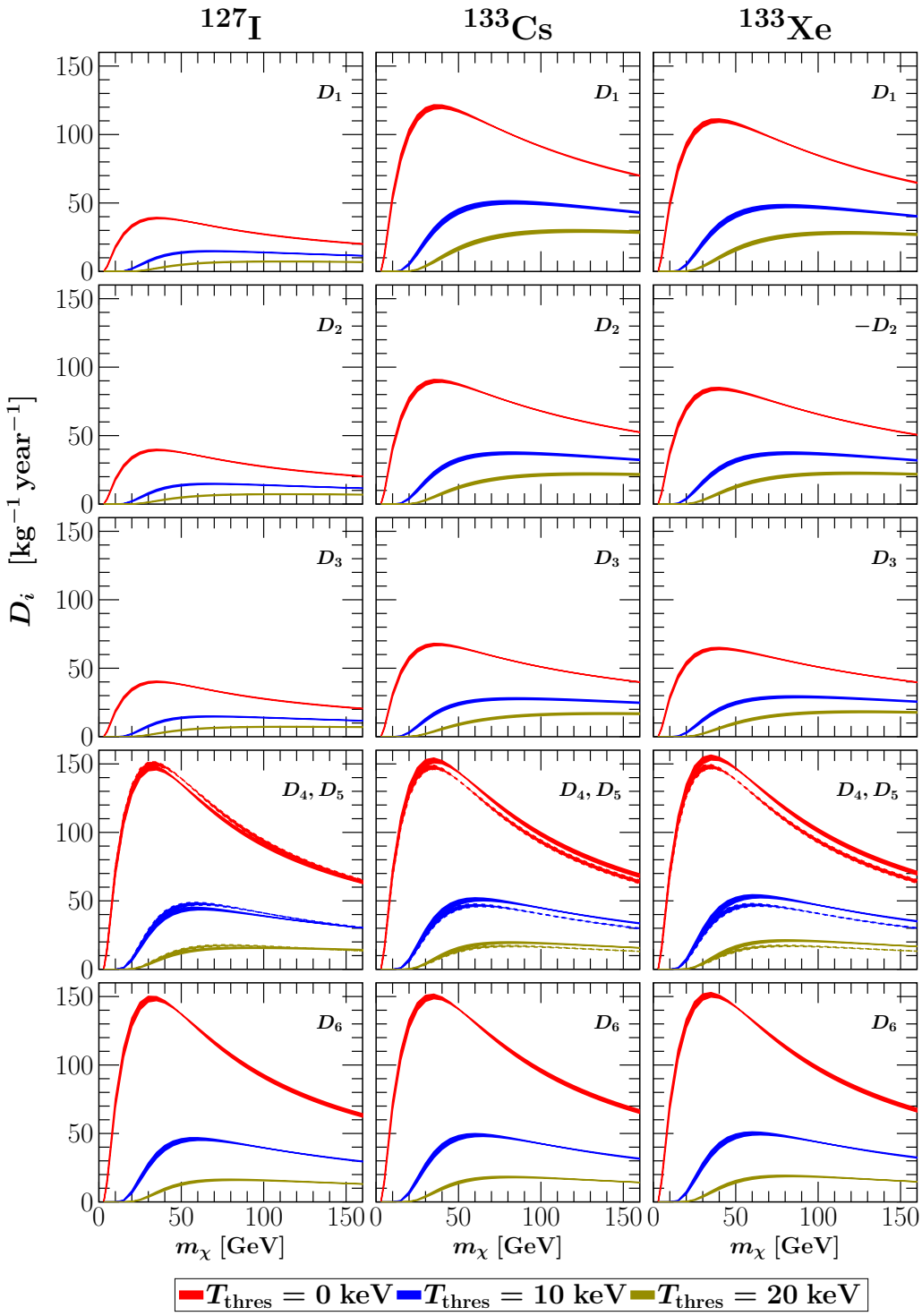

FIG. 4. Nuclear structure coefficients D_i, $i = 1, \ldots, 6$, as functions of the WIMP mass m_χ for the ^{127}I, ^{133}Cs, and ^{133}Xe isotopes. The results are evaluated for three values of the detector threshold, $T_{\rm thres} = 0$, 10, and 20 keV, while the thickness of the curves represents the annual modulation effect. Note that for the case of ^{133}Xe the coefficient D_2 is negative, while the coefficients D_5 are shown by thick dashed curves.

the value of Ω_1 is appreciably smaller (by a factor of 50). The spin structure functions $F_{\rho\rho'}$ relevant to inelastic scattering are plotted as functions of the dimensionless momentum transfer u in Fig. 6. It becomes evident from the plots that the values of F_{00}, F_{01}, and F_{11} are quite different from each other. Then the nuclear coefficients E_i are plotted in Fig. 7. At this point it is noteworthy that E_i do not depend on the detector threshold energy. As in the case of elastic scattering,

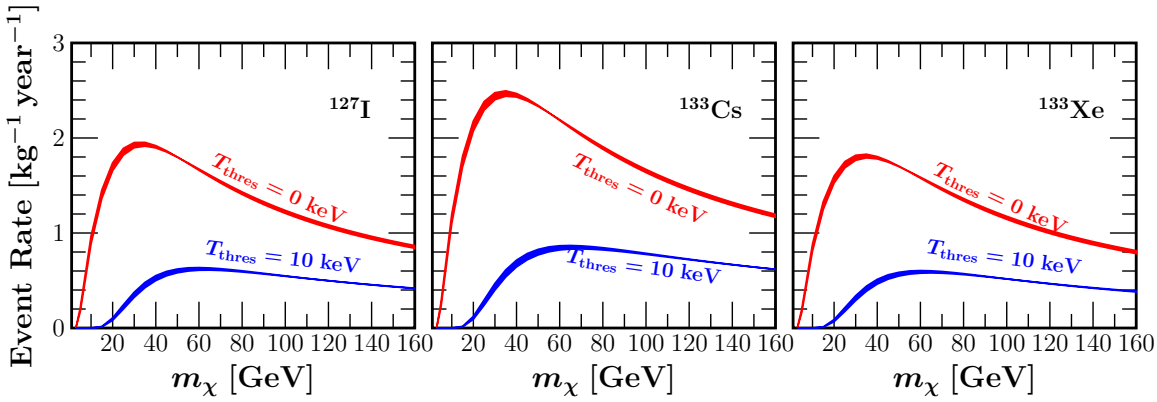

FIG. 5. Event rates due to elastic WIMP-nucleus scattering as a function of the DM mass m_χ for ^{127}I, ^{133}Cs, and ^{133}Xe at detector threshold $T_{\rm thres} = 0$ and 10 keV. The curve thickness represents the annual modulation effect.

the corresponding event rates due to inelastic transitions can be obtained by reading out the values of E_i from the figure and using the nucleonic current parameters and Eq. (15). Note that the calculated nuclear structure coefficients are almost of the same order of magnitude compared to the results given by Ref. [60], however, we predict a much smaller modulation effect. Similarly, the peak values of the nuclear structure coefficients occur at around $m_\chi = 70-80$ GeV, while in Ref. [60] it was found that the peaks occur at around $m_\chi \sim 200$ GeV.

For ^{133}Cs, the first excited state, having $J = 5/2^+$, is at energy 81 keV. Because of the closeness of this state to the ground state, for this nucleus also one may expect a large nucleon spin-induced cross section, leading to a nonnegligible probability for inelastic scattering to occur. The calculated static spin matrix elements Ω_0 and Ω_1 have values 0.020 and 0.041, respectively. These values are almost 40 times smaller than in the elastic case. The spin structure functions in the inelastic channel $7/2^+ \to 5/2^+$ are plotted as functions of u in Fig. 6. The graphs for F_{00}, F_{01}, and F_{11} are quite different from each other as in the case of ^{127}I. As shown in Fig. 7, the corresponding nuclear coefficients E_i for ^{133}Cs are in general smaller compared to those of ^{127}I. Finally, for ^{133}Xe, the lowest excited state is $J = 1/2^+$ and appears at 262 keV. The calculated static spin matrix elements Ω_0 and Ω_1 for the transition $3/2^+ \to 1/2^+$ are -0.031 and 0.013, i.e., more than 30 times smaller than the elastic case in this nucleus. The spin structure functions for this inelastic channel are plotted in Fig. 6, where one sees that the values of F_{00}, F_{01}, and F_{11} are quite different and show peaks. Finally, the nuclear coefficients E_i are plotted in Fig. 7, where it is shown that E_1, E_2, and E_3 are larger than those of ^{133}Cs, while the modulation effect is similar.

B. Results for neutrino-nucleus scattering

There are many interesting applications of low-energy neutrino scattering with nuclei that are of key importance to direct detection DM searches as shown in Ref. [5]. Apart from the fact that astrophysical neutrinos pose a significant background to DM searches, neutrino-nucleus scattering experiments are also relevant and complementary to the latter for a number of reasons. Among these, we mention that neutrino-nucleus experiments have opened a novel avenue to probe physics beyond the SM with a phenomenological impact on DM (see Ref. [6] and references therein). Moreover, it has recently been shown that accelerator-produced DM can be detected in CEνNS experiments [78]. Finally, CEνNS experiments can be used to probe the nuclear structure as well as to characterize the nuclear responses of the same target material employed in direct detection DM experiments.

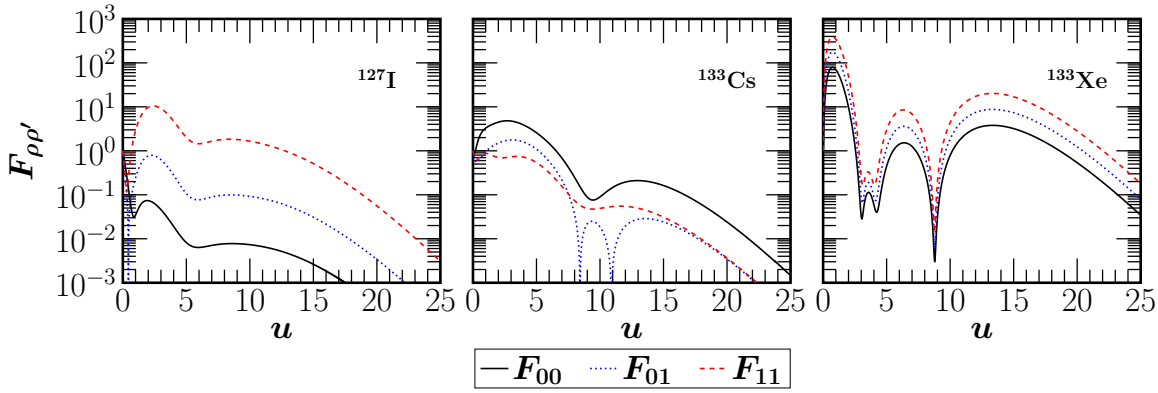

FIG. 6. Spin structure function in the inelastic channel for ^{127}I, ^{133}Cs, and ^{133}Xe.

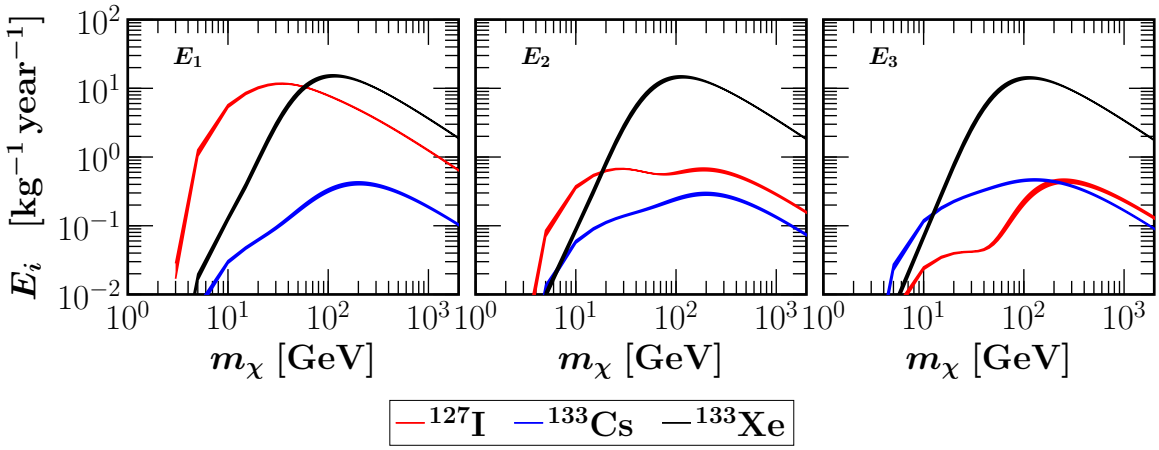

FIG. 7. Nuclear structure coefficients E_i, $i = 1, 2, 3$, in the inelastic channel of ^{127}I, ^{133}Cs, and ^{133}Xe. The thickness of the curves represents the annual modulation effect. For the case of ^{133}Xe the coefficient E_2 is negative.

In this section, our calculations refer to laboratory ν sources (reactor and pion decay at rest; π-DAR) and astrophysical (solar) neutrino sources having an evident connection to our previous results regarding WIMP-nucleus scattering [5]. We focus on popular nuclear targets employed in current and future neutrino-nucleus and DM scattering experiments. To this end, using the DSM we calculate the differential and integrated event rates due to CEνNS and IνNS assuming SM interactions only, as

$$\frac{dR_x}{dT_A} = \mathcal{K}\int_{E_\nu^{\min}}^{E_\nu^{\max}} \frac{d\sigma_x}{dT_A}(E_\nu, T_A)\lambda_\nu(E_\nu)\,dE_\nu, \quad x = \text{coh, inc}, \tag{31}$$

where $\lambda_\nu(E_\nu)$ represents the relevant neutrino energy distribution function characterizing the neutrino source. The normalization factor $\mathcal{K} = t_{\text{run}}\Phi_\nu N_{\text{targ}}$ depends on the exposure time, the neutrino flux, and the number of target nuclei. Our goal is to compare the nuclear responses between the various chosen isotopes for CEνNS and IνNS processes. To achieve a more direct comparison, we relax ourselves from being experiment specific, but rather in our calculations we assume the same detector mass and exposure time for all nuclear targets. Specifically, for reactor- and π-DAR-based neutrino experiments we consider 1 kg of detector mass and 1 year of data-taking, while for the case of direct DM detection experiments we assume 1 ton of detector mass and 1 year of running time.

We begin our calculational procedure by considering the CEνNS and IνNS channels in the case of neutrino experiments utilizing π-DAR neutrinos, like the COHERENT at the SNS (the ESS [8] is another promising possibility). It has recently been shown that a better agreement between the SM expectation and the COHERENT data is possible through DSM calculations [4], while reasonable constraints on nuclear physics parameters have been placed from the COHERENT data [79,80]. The relevant nuclear isotopes are ^{133}Cs and ^{127}I, i.e., the detector materials used during the first run of COHERENT with a CsI detector that led to the first observation of CEνNS [1,81]. By assuming a typical SNS neutrino flux of $\Phi_\nu \sim 10^7\ \nu\,\text{cm}^{-2}\,\text{s}^{-1}$ and a threshold of 100 eV we calculate the differential event rates and the number of events above threshold. The corresponding results are presented in Fig. 8 for ^{127}I, ^{133}Cs, and ^{133}Xe. In this figure it can be seen that the CEνNS channel dominates the expected signal by at least 1 order of magnitude. However, the IνNS channel can be detectable in the high-energy tail of the recoil spectrum, i.e., a possible excess in the spectral shape distribution for high recoil energies is due to potential IνNS contributions. We also consider the ^{40}Ar nucleus, which has been employed by the CENNS-10 liquid argon (LAr) detector subsystem [82], and recently detected CEνNS with more than 3σ significance [2], leading to improved constraints on various parameters with regard to neutrino physics within and beyond the SM [80]. Finally, our calculations also include the ^{73}Ge and ^{23}Na nuclei, which are the target material of the next-generation detectors that will be deployed in the *Neutrino Alley* at the SNS [7]. The respective results for ^{23}Na, ^{40}Ar, and ^{73}Ge are depicted in Fig. 9, leading to the same general conclusions as for the heavier isotopes. In all cases, kinks appear at maximum recoil energies (different for each nuclear isotope) due to prompt-neutrino scattering.

We now turn our discussion to promising reactor-based experiments looking for neutrino-nucleus events. Recently, there has been a very active experimental effort with new experiments aiming to measure CEνNS [46]. Novel developments and instrumentation based on cutting-edge technologies are currently pursued in order to reduce the detection threshold in the sub-keV region. The most interesting nuclear isotope is ^{73}Ge, which constitutes the main target material of the CONUS [9], CONNIE [10], MINER [11], NU-CLEUS [15], Ricochet [14], vGEN [83], and TEXONO [84] experiments. It is noteworthy that the ^{133}Xe isotope is another interesting target, being the target nucleus of the RED100 [85] experiment. By assuming a reactor antineutrino flux of $\Phi_\nu \sim 10^{13}\ \nu\,\text{cm}^{-2}\,\text{s}^{-1}$ we illustrate the corresponding differential and integrated event rates as a function of the nuclear recoil energy in Figs. 10 and 11. Contrary to the SNS case discussed previously, it becomes evident that the CEνNS rate dominates over the IνNS channel by 2–3 orders of magnitude. As expected, the IνNS channel is not relevant due to the very

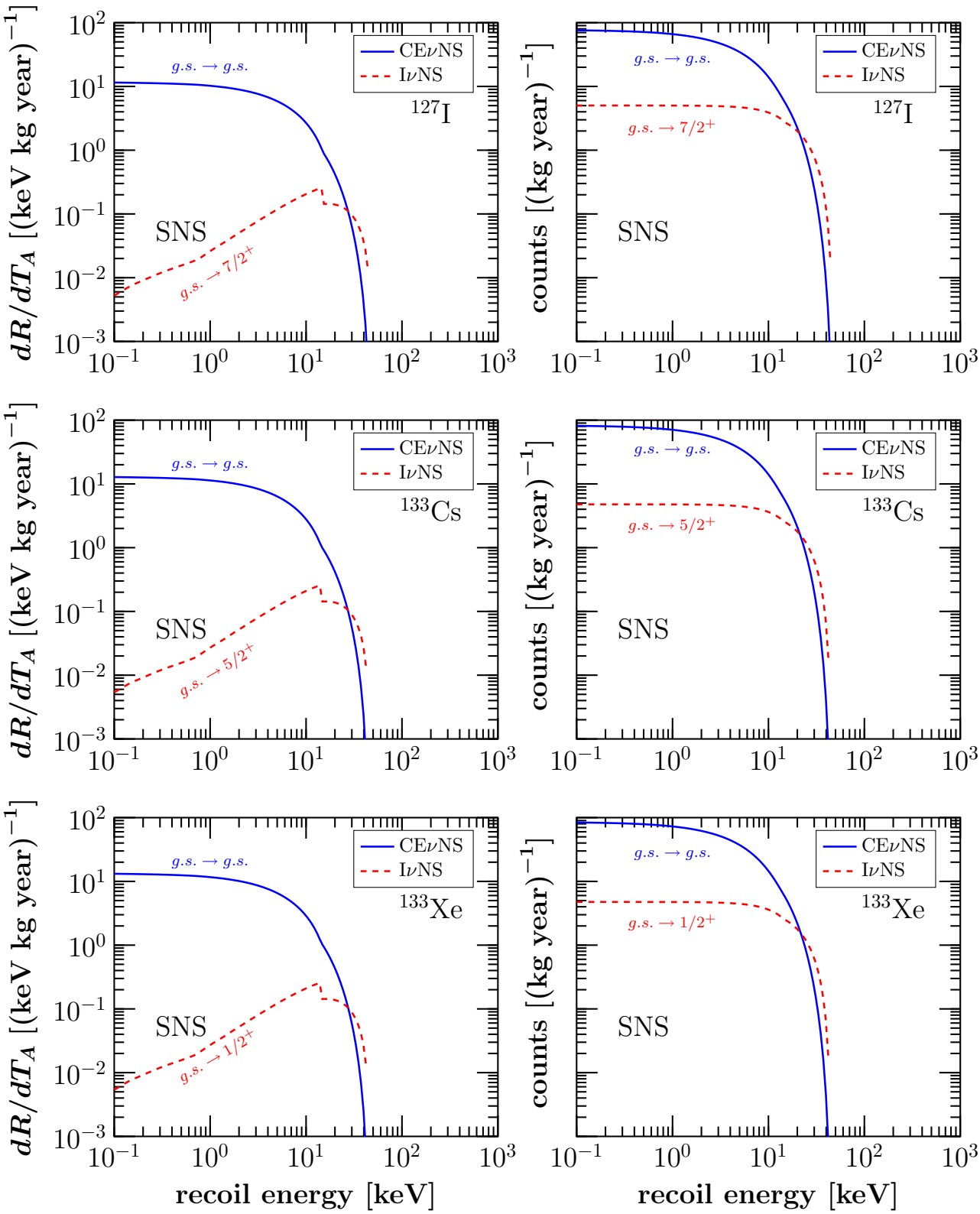

FIG. 8. Differential (left) and integrated (right) event rates as a function of the nuclear recoil energy for ^{127}I, ^{133}Cs, and ^{133}Xe. The results are presented for CEνNS and IνNS processes with π-DAR neutrinos.

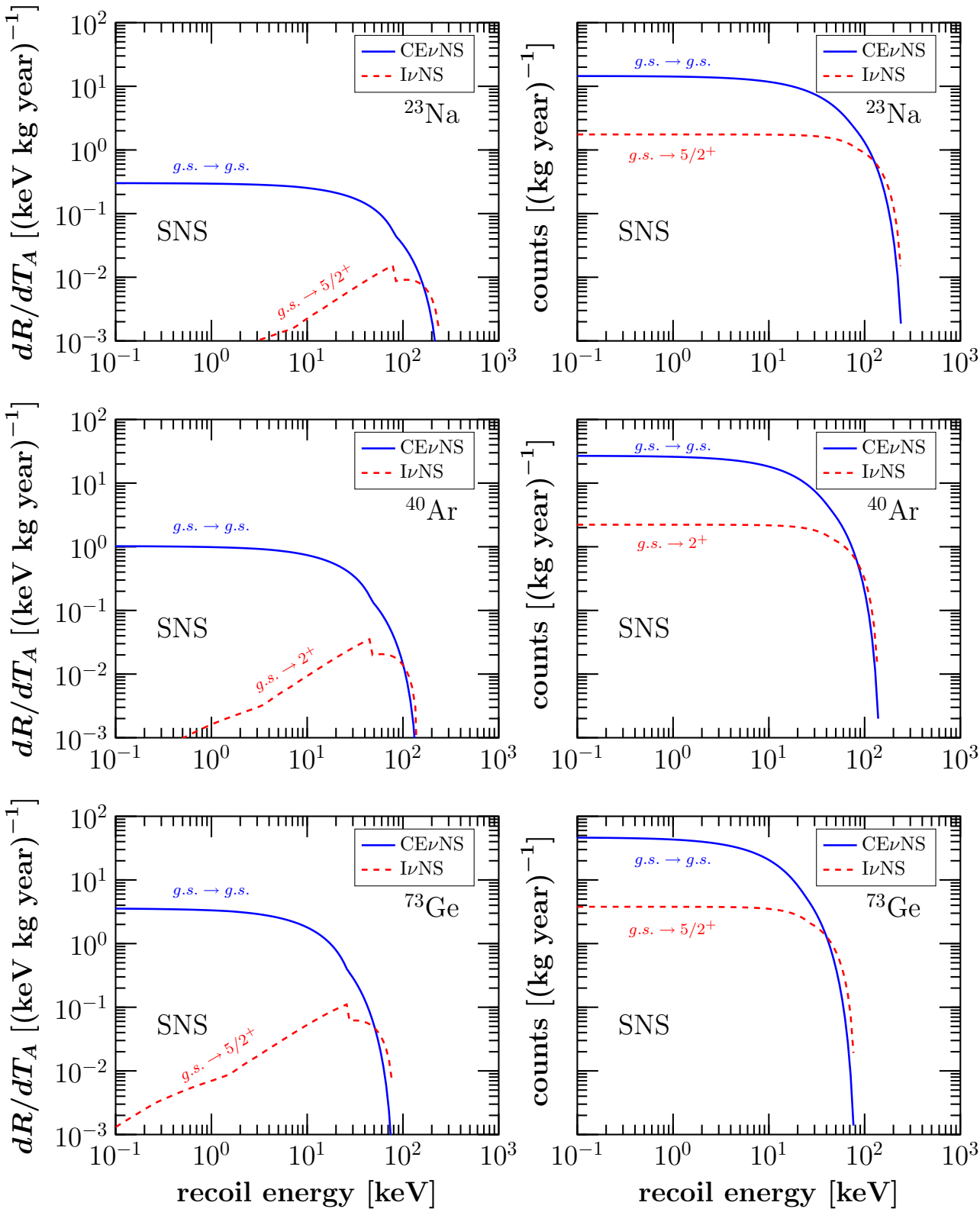

FIG. 9. Same as Fig. 8, but for ^{23}Na, ^{40}Ar, and ^{73}Ge.

low momentum transfer occurring when low-energy reactor antineutrinos scatter off nuclei, i.e., the $1 - F_f(|\mathbf{q}|)$ factor becomes tiny, leading to an appreciable suppression of the incoherent cross section.

Finally, we study CEνNS and IνNS processes due to nuclear interactions of neutrinos at ton-scale direct DM detectors. The latter constitute an irreducible background to WIMP-nucleus scattering events in direct detection DM

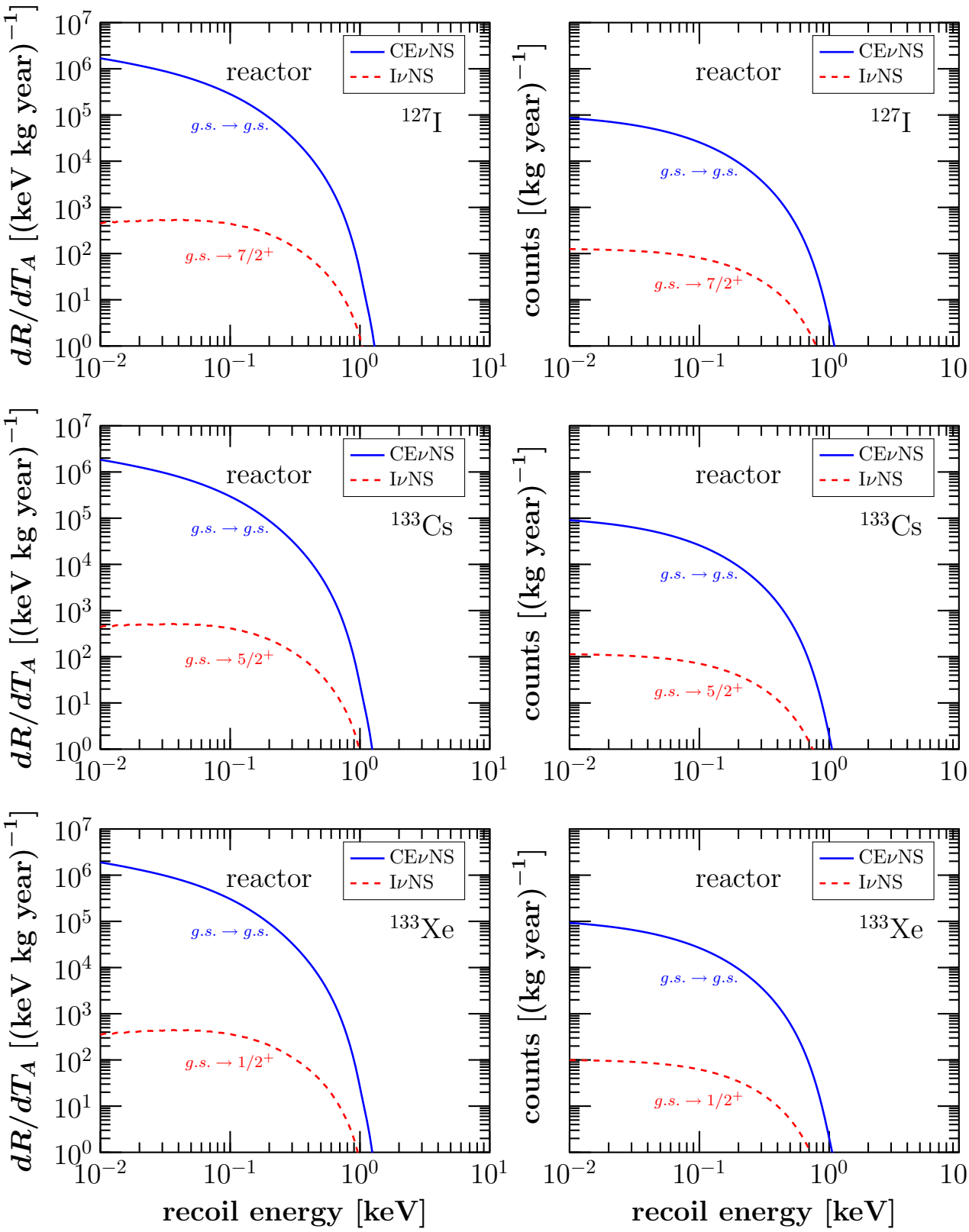

FIG. 10. Differential (left) and integrated (right) event rates as a function of the nuclear recoil energy for ^{127}I, ^{133}Cs, and ^{133}Xe. The results are presented for CEνNS and IνNS processes with reactor neutrinos.

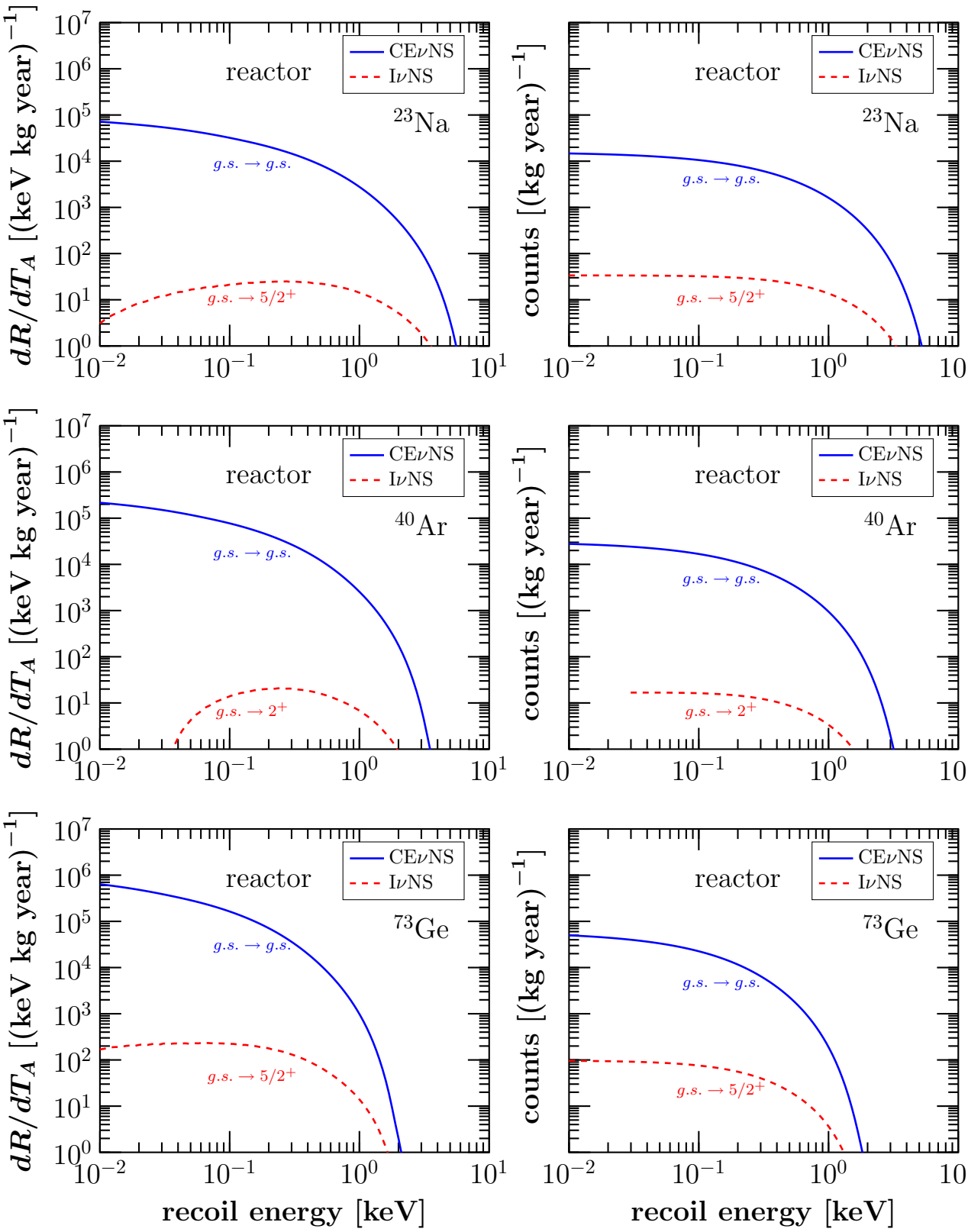

FIG. 11. Same as Fig. 10, but for ^{23}Na, ^{40}Ar, and ^{73}Ge.

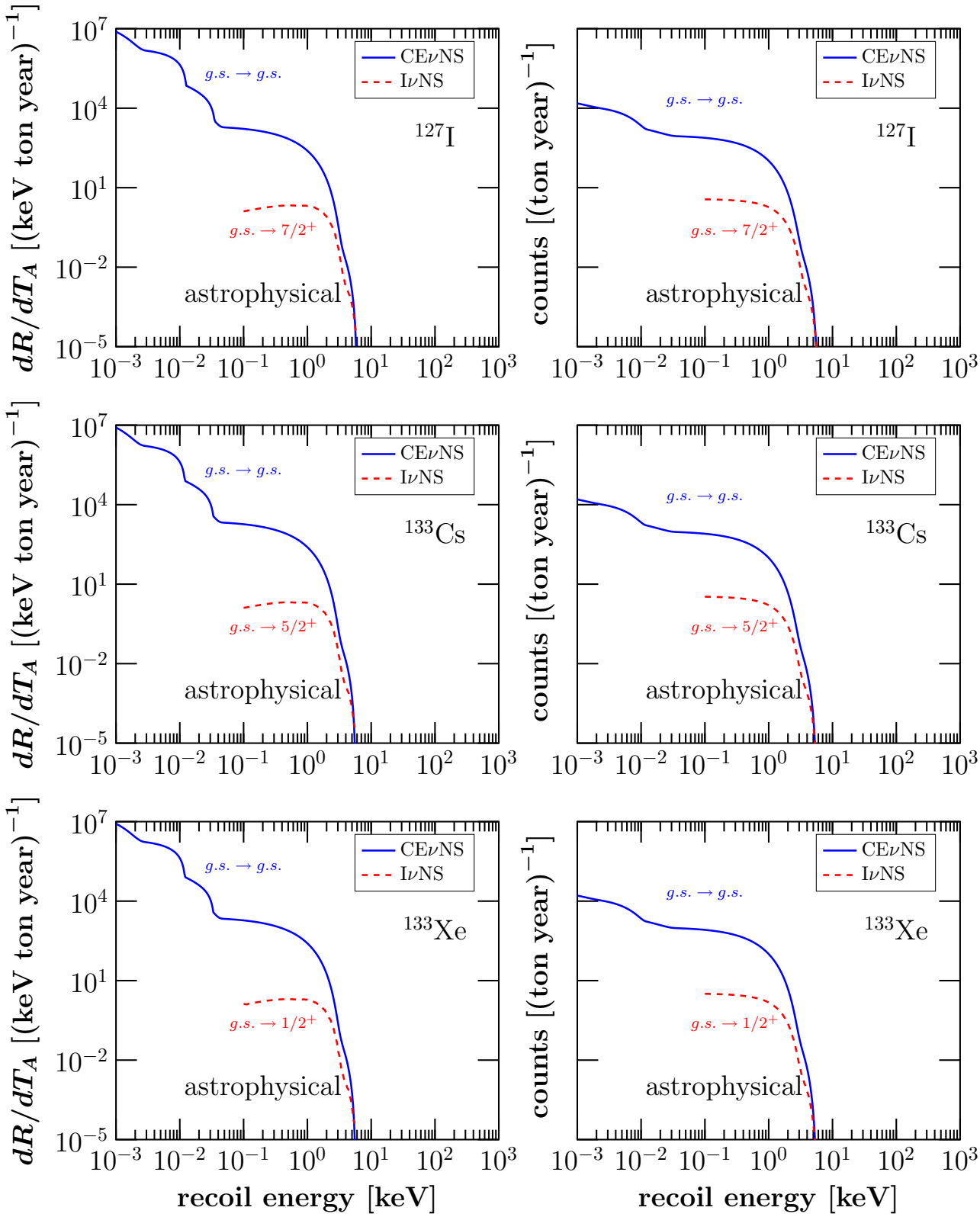

FIG. 12. Differential (left) and integrated (right) event rates as a function of the nuclear recoil energy for ^{127}I, ^{133}Cs, and ^{133}Xe. The results are presented for CEνNS and IνNS processes with solar neutrinos.

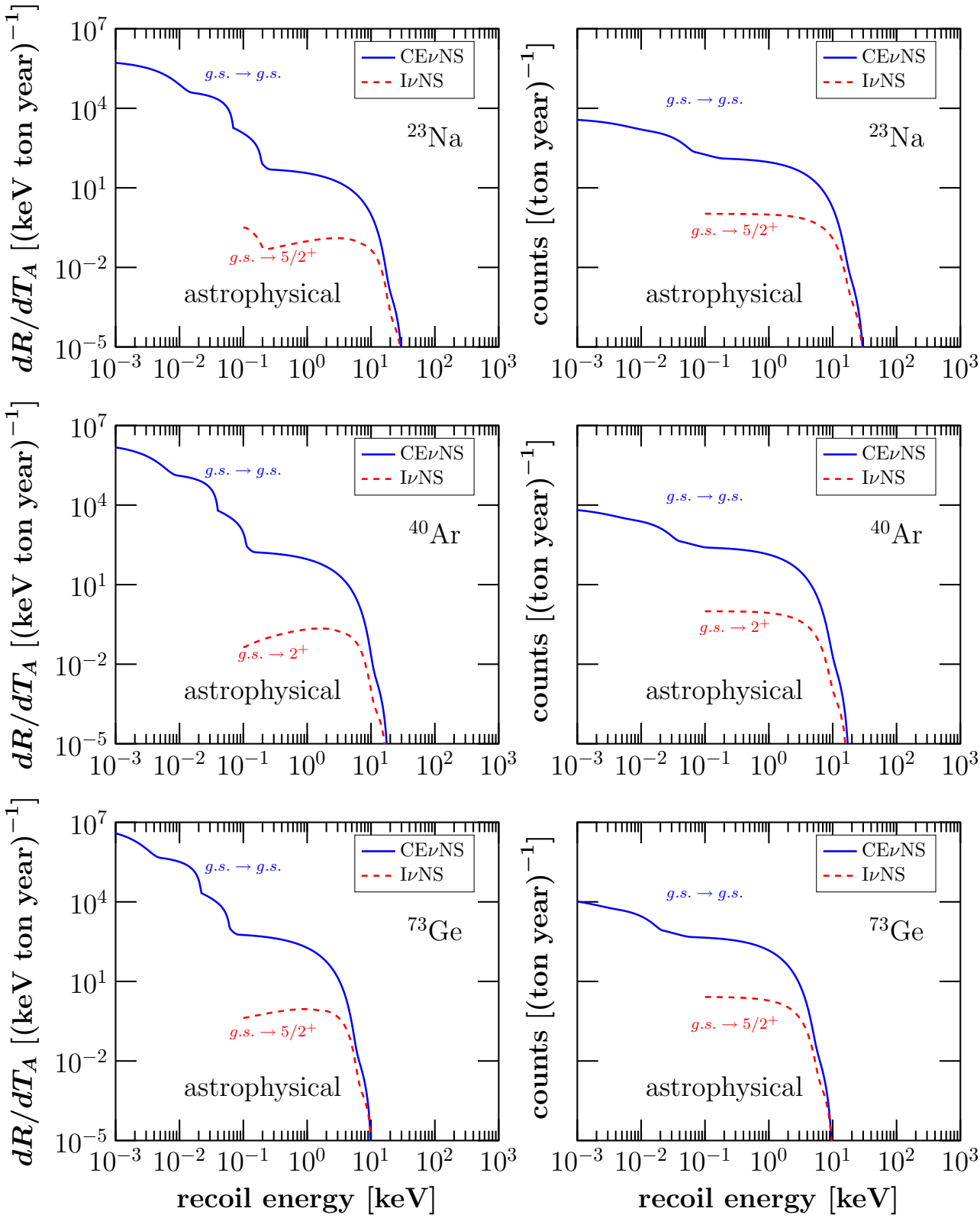

FIG. 13. Same as Fig. 12, but for ^{23}Na, ^{40}Ar, and ^{73}Ge.

searches, also known as the neutrino floor [47]. Indeed, a neutrino-induced event can mimic a potential WIMP-nucleus signal, which may subsequently lead to an erroneous interpretation of DM observation. Moreover, it has been noted recently that existing uncertainties in the SM event rate, mainly those coming from the nuclear form factor, require further attention [5,52]. For this reason, in this work a comprehensive calculation that takes into account realistic nuclear

structure calculations through the DSM, as well as the nuclear responses from both CEνNS and IνNS interactions, is performed. Furthermore, since we are interested in low-threshold detectors we restrict ourselves to solar neutrinos only, without including the contributions due to atmospheric and DSNB neutrinos. The combined effect of the large energy-related uncertainties characterizing the atmospheric and DSNB neutrino spectra, in conjunction with the corresponding ones regarding the form factors at large momentum transfer, stand out as another motivation for this assumption. The target nuclei of interest are ^{40}Ar (DarkSide [21], DEAP-3600 [22]), ^{73}Ge (CDEX, SuperCDMS [25]), and ^{133}Xe (LUX [26], XENON1T [27], DARWin Ref. [28], PandaX-II [29]). Our DSM results are presented in Figs. 12 and 13. As expected, the IνNS rate coming from the low-energy solar neutrino spectra is subdominant with respect to the CEνNS rate. On the other hand, this may not be the case when atmospheric and DSNB neutrinos are taken into account. As mentioned previously, the expected IνNS rates for high-energy neutrinos and at high momentum transfer require special attention that goes beyond the scope of this study. Such results are in progress and will be published in a future work.

VI. SUMMARY AND CONCLUSIONS

In this study we have presented the expected neutrino-nucleus and WIMP-nucleus events at prominent rare-event detectors, calculated in the framework of the deformed shell model. The chosen nuclear isotopes, ^{23}Na, ^{40}Ar, ^{73}Ge, ^{127}I, ^{133}Cs, and ^{133}Xe, were carefully selected to correspond to present and future experiments looking for CEνNS events and WIMP candidates at direct detection dark-matter detectors.

The nuclear effects being probably the largest source of theoretical uncertainty are limiting the potential of the relevant experiments in placing constraints on physics beyond the SM. In this work, the addressed corrections coming from nuclear structure are adequately taken into consideration through the DSM and are essential to accurately simulate the expected event rates. In particular, on the basis of Hartree-Fock nuclear states, we have conducted a comprehensive study by also taking into account the deformation of the studied nuclear isotopes, leading to a more accurate determination of the spin nuclear structure function and the nuclear form factors for protons and neutrons.

We have, furthermore, illustrated a comparison of the relevant magnitude between the coherent and the incoherent processes as well as their recoil energy dependence assuming various neutrino sources. Our obtained results indicate that incoherent neutrino-nucleus processes can lead to an observable enhancement of the expected signal that is well above the energy threshold at multiton direct detection dark-matter detectors. Similarly a corresponding enhancement was found for the case of WIMP-nucleus scattering. We have finally emphasized that in both cases a signal coming from the deexcitation gammas in the aftermath of an incoherent processes can be erroneously misinterpreted as a possible new physics signature.

ACKNOWLEDGMENTS

The research of D.K.P. was cofinanced by Greece and the European Union (European Social Fund; ESF) through the Operational Programme Human Resources Development, Education and Lifelong Learning in the context of the project "Reinforcement of Postdoctoral Researchers—2nd Cycle" (MIS-5033021), implemented by the State Scholarships Foundation (IKY). R.S. is thankful to SERB of the Department of Science and Technology (Government of India) for financial support. The work of T.S.K. was implemented through the Operational Program "Human Resources Development, Education and Lifelong Learning—Cycle B" (MIS-5047635) and was cofinanced by the European Union (ESF) and Greek national funds.

[1] D. Akimov *et al.* (COHERENT Collaboration), Observation of coherent elastic neutrino-nucleus scattering, Science **357**, 1123 (2017).

[2] D. Akimov *et al.* (COHERENT Collaboration), First detection of coherent elastic neutrino-nucleus scattering on argon, arXiv:2003.10630 [nucl-ex].

[3] V. A. Bednyakov and D. V. Naumov, Coherency and incoherency in neutrino-nucleus elastic and inelastic scattering, Phys. Rev. D **98**, 053004 (2018).

[4] D. K. Papoulias, T. S. Kosmas, R. Sahu, V. K. B. Kota, and M. Hota, Constraining nuclear physics parameters with current and future COHERENT data, Phys. Lett. B **800**, 135133 (2020).

[5] D. K. Papoulias, R. Sahu, T. S. Kosmas, V. K. B. Kota, and B. Nayak, Novel neutrino-floor and dark matter searches with deformed shell model calculations, Adv. High Energy Phys. **2018**, 6031362 (2018).

[6] D. K. Papoulias, T. S. Kosmas, and Y. Kuno, Recent probes of standard and non-standard neutrino physics with nuclei, Front. Phys. **7**, 191 (2019).

[7] D. Akimov *et al.* (COHERENT Collaboration), COHERENT 2018 at the Spallation Neutron Source, arXiv:1803.09183 [physics.ins-det].

[8] D. Baxter *et al.*, Coherent elastic neutrino-nucleus scattering at the European Spallation Source, J. High Energy Phys. 02 (2020) 123.

[9] J. Hakenmüller *et al.*, Neutron-induced background in the CONUS experiment, Eur. Phys. J. C **79**, 699 (2019).

[10] A. Aguilar-Arevalo *et al.* (CONNIE Collaboration), Exploring low-energy neutrino physics with the Coherent Neutrino Nucleus Interaction Experiment, Phys. Rev. D **100**, 092005 (2019).

[11] G. Agnolet *et al.* (MINER Collaboration), Background studies for the MINER coherent neutrino scattering reactor experiment, Nucl. Instrum. Methods A **853**, 53 (2017).

[12] H. T. Wong, Neutrino-nucleus coherent scattering and dark matter searches with sub-keV germanium detector, Nucl. Phys. A **844**, 229C (2010).

[13] D. Akimov *et al.*, RED-100 detector for the first observation of the elastic coherent neutrino scattering off xenon nuclei, J. Phys. Conf. Ser. **675**, 012016 (2016).
[14] J. Billard *et al.*, Coherent neutrino scattering with low temperature bolometers at Chooz reactor complex, J. Phys. G **44**, 105101 (2017).
[15] G. Angloher *et al.* (NUCLEUS Collaboration), Exploring CEνNS with NUCLEUS at the Chooz nuclear power plant, Eur. Phys. J. C **79**, 1018 (2019).
[16] O. Moreno, E. Moya de Guerra, and M. R. Medrano, Warm dark matter sterile neutrinos in electron capture and beta decay spectra, Adv. High Energy Phys. **2016**, 6318102 (2016).
[17] J. A. Dror, G. Elor, and R. Mcgehee, Directly Detecting Signals from Absorption of Fermionic Dark Matter, Phys. Rev. Lett. **124**, 181301 (2020).
[18] J. A. Dror, G. Elor, and R. Mcgehee, Absorption of fermionic dark matter by nuclear targets, J. High Energy Phys. 02 (2020) 134.
[19] M. Kortelainen, J. Suhonen, J. Toivanen, and T. S. Kosmas, Event rates for CDM detectors from large-scale shell-model calculations, Phys. Lett. B **632**, 226 (2006).
[20] G. Jungman, M. Kamionkowski, and K. Griest, Supersymmetric dark matter, Phys. Rep. **267**, 195 (1996).
[21] P. Agnes *et al.* (DarkSide Collaboration), Constraints on Sub-GeV Dark-Matter-Electron Scattering from the DarkSide-50 Experiment, Phys. Rev. Lett. **121**, 111303 (2018).
[22] P. A. Amaudruz *et al.* (DEAP-3600 Collaboration), First Results from the DEAP-3600 Dark Matter Search with Argon at SNOLAB, Phys. Rev. Lett. **121**, 071801 (2018).
[23] L. Yang *et al.* (CDEX Collaboration), Search for Light Weakly-Interacting-Massive-Particle Dark Matter by Annual Modulation Analysis with A Point-Contact Germanium Detector at the China Jinping Underground Laboratory, Phys. Rev. Lett. **123**, 221301 (2019).
[24] Z. Liu *et al.* (CDEX Collaboration), Constraints on Spin-Independent Nucleus Scattering with Sub-GeV Weakly Interacting Massive Particle Dark Matter from the CDEX-1B Experiment at the China Jinping Underground Laboratory, Phys. Rev. Lett. **123**, 161301 (2019).
[25] R. Agnese *et al.* (SuperCDMS Collaboration), Projected sensitivity of the SuperCDMS SNOLAB experiment, Phys. Rev. D **95**, 082002 (2017).
[26] D. S. Akerib *et al.* (LUX Collaboration), Results from A Search for Dark Matter in the Complete LUX Exposure, Phys. Rev. Lett. **118**, 021303 (2017).
[27] E. Aprile *et al.* (XENON Collaboration), Physics reach of the XENON1T dark matter experiment, J. Cosmol. Astropart. Phys. 04 (2016) 027.
[28] J. Aalbers *et al.* (DARWIN Collaboration), DARWIN: Towards the ultimate dark matter detector, J. Cosmol. Astropart. Phys. 11 (2016) 017.
[29] C. Fu *et al.* (PandaX-II Collaboration), Spin-Dependent Weakly-Interacting-Massive-Particle-Nucleon Cross Section Limits from First Data of PandaX-II Experiment, Phys. Rev. Lett. **118**, 071301 (2017); **120**, 049902(E) (2018).
[30] T. S. Kosmas and J. D. Vergados, Cold dark matter in SUSY theories. The role of nuclear form-factors and the folding with the LSP velocity, Phys. Rev. D **55**, 1752 (1997).
[31] G. F. Smoot *et al.* (COBE Collaboration), Structure in the COBE differential microwave radiometer first year maps, Astrophys. J. **396**, L1 (1992).
[32] E. Gawiser and J. Silk, Extracting primordial density fluctuations, Science **280**, 1405 (1998).
[33] G. Hinshaw *et al.* (WMAP Collaboration), Nine-year Wilkinson microwave anisotropy probe (WMAP) observations: Cosmological parameter results, Astrophys. J. Suppl. **208**, 19 (2013).
[34] N. Aghanim *et al.* (Planck Collaboration), Planck 2018 results. VI. Cosmological parameters, arXiv:1807.06209 [astro-ph.CO].
[35] K. Freese, M. Lisanti, and C. Savage, Colloquium: Annual modulation of dark matter, Rev. Mod. Phys. **85**, 1561 (2013).
[36] J. Liu, X. Chen, and X. Ji, Current status of direct dark matter detection experiments, Nature Phys. **13**, 212 (2017).
[37] R. Sahu and V. K. B. Kota, Deformed shell model study of event rates for WIMP-^{73}Ge scattering, Mod. Phys. Lett. A **32**, 1750210 (2017).
[38] E. Aprile *et al.* (XENON Collaboration), Dark Matter Search Results from A One Ton-Year Exposure of XENON1T, Phys. Rev. Lett. **121**, 111302 (2018).
[39] C. Amole *et al.* (PICO Collaboration), Dark Matter Search Results from the PICO-60 C_3F_8 Bubble Chamber, Phys. Rev. Lett. **118**, 251301 (2017).
[40] A. Broniatowski *et al.*, A new high-background-rejection dark matter Ge cryogenic detector, Phys. Lett. B **681**, 305 (2009).
[41] N. Du *et al.* (ADMX Collaboration), A Search for Invisible Axion Dark Matter with the Axion Dark Matter Experiment, Phys. Rev. Lett. **120**, 151301 (2018).
[42] S. C. Kim, H. Bhang, J. H. Choi, W. G. Kang, B. H. Kim, H. J. Kim, K. W. Kim, S. K. Kim, Y. D. Kim, J. Lee, J. H. Lee, J. K. Lee, M. J. Lee, S. J. Lee, J. Li, J. Li, X. R. Li, Y. J. Li, S. S. Myung, S. L. Olsen, S. Ryu, I. S. Seong, J. H. So, and Q. Yue, New Limits on Interactions between Weakly Interacting Massive Particles and Nucleons Obtained with CsI(Tl) Crystal Detectors, Phys. Rev. Lett. **108**, 181301 (2012).
[43] R. Bernabei *et al.*, Final model independent result of DAMA/LIBRA-phase1, Eur. Phys. J. C **73**, 2648 (2013).
[44] E. Behnke *et al.* (COUPP Collaboration), First dark matter search results from a 4-kg CF_3I bubble chamber operated in a deep underground site, Phys. Rev. D **86**, 052001 (2012); **90**, 079902(E) (2014).
[45] P. C. Divari, T. S. Kosmas, J. D. Vergados, and L. D. Skouras, Shell model calculations for light supersymmetric particle scattering off light nuclei, Phys. Rev. C **61**, 054612 (2000).
[46] D. Yu. Akimov, V. A. Belov, A. Bolozdynya, Yu. V. Efremenko, A. M. Konovalov, A. V. Kumpan, D. G. Rudik, V. V. Sosnovtsev, A. V. Khromov, and A. V. Shakirov, Coherent elastic neutrino scattering on atomic nucleus: Recently discovered type of low-energy neutrino interaction, Phys. Usp. **62**, 166 (2019).
[47] J. Billard, L. Strigari, and E. Figueroa-Feliciano, Implication of neutrino backgrounds on the reach of next generation dark matter direct detection experiments, Phys. Rev. D **89**, 023524 (2014).
[48] C. A. O'Hare, Dark matter astrophysical uncertainties and the neutrino floor, Phys. Rev. D **94**, 063527 (2016).
[49] C. Bœhm, D. Cerdeño, P. Machado, A. Olivares-Del Campo, E. Perdomo, and E. Reid, How high is the neutrino floor? J. Cosmol. Astropart. Phys. 01 (2019) 043.
[50] C. A. O'Hare, Can we overcome the neutrino floor at high masses? arXiv:2002.07499 [astro-ph.CO].

[51] D. Aristizabal Sierra, B. Dutta, S. Liao, and L. E. Strigari, Coherent elastic neutrino-nucleus scattering in multi-ton scale dark matter experiments: Classification of vector and scalar interactions new physics signals, J. High Energy Phys. 12 (2019) 124.

[52] D. Aristizabal Sierra, J. Liao, and D. Marfatia, Impact of form factor uncertainties on interpretations of coherent elastic neutrino-nucleus scattering data, J. High Energy Phys. 06 (2019) 141.

[53] D. Papoulias and T. Kosmas, Standard and non-standard neutrino-nucleus reactions cross sections and event rates to neutrino detection experiments, Adv. High Energy Phys. **2015**, 763648 (2015).

[54] P. Pirinen, J. Suhonen, and E. Ydrefors, Neutral-current neutrino-nucleus scattering off Xe isotopes, Adv. High Energy Phys. **2018**, 9163586 (2018).

[55] C. G. Payne, S. Bacca, G. Hagen, W. G. Jiang, and T. Papenbrock, Coherent elastic neutrino-nucleus scattering on ^{40}Ar from first principles, Phys. Rev. C **100**, 061304(R) (2019).

[56] G. Co', M. Anguiano, and A. Lallena, Nuclear structure uncertainties in coherent elastic neutrino-nucleus scattering, J. Cosmol. Astropart. Phys. 04 (2020) 044.

[57] N. Van Dessel, V. Pandey, H. Ray, and N. Jachowicz, Nuclear structure physics in coherent elastic neutrino-nucleus scattering, arXiv:2007.03658 [nucl-th].

[58] J. D. Vergados, Modulation Effect with Realistic Velocity Dispersion of Supersymmetric Dark Matter, Phys. Rev. Lett. **83**, 3597 (1999).

[59] E. Holmlund, M. Kortelainen, T. S. Kosmas, J. Suhonen, and J. Toivanen, Microscopic calculation of the LSP detection rates for the Ga-71, Ge-73, and I-127 dark-matter detectors, Phys. Lett. B **584**, 31 (2004).

[60] P. Toivanen, M. Kortelainen, J. Suhonen, and J. Toivanen, Large-scale shell-model calculations of elastic and inelastic scattering rates of lightest supersymmetric particles (LSP) on I-127, Xe-129, Xe-131, and Cs-133 nuclei, Phys. Rev. C **79**, 044302 (2009).

[61] P. Pirinen, P. C. Srivastava, J. Suhonen, and M. Kortelainen, Shell-model study on event rates of lightest supersymmetric particles scattering off ^{83}Kr and ^{125}Te, Phys. Rev. D **93**, 095012 (2016).

[62] J. D. Vergados, C. C. Moustakidis, Y.-K. E. Cheung, H. Ejri, Y. Kim, and Y. Lie, Light WIMP searches involving electron scattering, Adv. High Energy Phys. **2018**, 6257198 (2018).

[63] J. Menéndez, D. Gazit, and A. Schwenk, Spin-dependent WIMP scattering off nuclei, Phys. Rev. D **86**, 103511 (2012).

[64] P. Klos, J. Menéndez, D. Gazit, and A. Schwenk, Large-scale nuclear structure calculations for spin-dependent WIMP scattering with chiral effective field theory currents, Phys. Rev. D **88**, 083516 (2013); **89**, 029901(E) (2014).

[65] L. Baudis, G. Kessler, P. Klos, R. F. Lang, J. Menéndez, S. Reichard, and A. Schwenk, Signatures of dark matter scattering inelastically off nuclei, Phys. Rev. D **88**, 115014 (2013).

[66] L. Vietze, P. Klos, J. Menéndez, W. C. Haxton, and A. Schwenk, Nuclear structure aspects of spin-independent WIMP scattering off xenon, Phys. Rev. D **91**, 043520 (2015).

[67] V. K. B. Kota and R. Sahu, *Structure of Medium Mass Nuclei: Deformed Shell Model and Spin-Isospin Interacting Boson Model* (CRC Press, Boca Raton, FL, 2016).

[68] P. C. Srivastava, R. Sahu, and V. K. B. Kota, Shell model and deformed shell model spectroscopy of ^{62}Ga, Eur. Phys. J. A **51**, 3 (2015).

[69] R. Sahu, P. C. Srivastava, and V. K. B. Kota, Deformed shell model results for neutrinoless positron double beta decay of nuclei in the $A = 60-90$ region, J. Phys. G **40**, 095107 (2013).

[70] R. Sahu and V. K. B. Kota, Deformed shell model results for neutrinoless double beta decay of nuclei in $A = 60-90$ region, Int. J. Mod. Phys. E **24**, 1550022 (2015).

[71] T. S. Kosmas, A. Faessler, and R. Sahu, Transition matrix elements for μe conversion in Ge-72 using the deformed Hartree-Fock method, Phys. Rev. C **68**, 054315 (2003).

[72] R. Sahu and V. K. B. Kota, Deformed shell model for $t = 0$ and $t = 1$ bands in Ga-62 and As-66, Phys. Rev. C **66**, 024301 (2002).

[73] R. Sahu and V. K. B. Kota, Deformed shell model for collective $T = 0$ and $T = 1$ bands in V-46 and Mn-50, Phys. Rev. C **67**, 054323 (2003).

[74] http://www.nndc.bnl.gov/ensdf.

[75] L. Coraggio, L. De Angelis, T. Fukui, A. Gargano, and N. Itaco, Calculation of Gamow-Teller and two-neutrino double-β decay properties for ^{130}Te and ^{136}Xe with a realistic nucleon-nucleon potential, Phys. Rev. C **95**, 064324 (2017).

[76] B. Ding *et al.*, High-spin states in I-127, Phys. Rev. C **85**, 044306 (2012).

[77] J. D. Vergados, Searching for cold dark matter, J. Phys. G **22**, 253 (1996).

[78] D. Akimov *et al.* (COHERENT Collaboration), Sensitivity of the COHERENT experiment to accelerator-produced dark matter, arXiv:1911.06422 [hep-ex].

[79] M. Cadeddu, C. Giunti, Y. Li, and Y. Zhang, Average CsI Neutron Density Distribution from COHERENT Data, Phys. Rev. Lett. **120**, 072501 (2018).

[80] O. Miranda, D. Papoulias, G. S. Garcia, O. Sanders, M. Tórtola, and J. Valle, Implications of the first detection of coherent elastic neutrino-nucleus scattering (CEvNS) with liquid argon, J. High Energy Phys. 05 (2020) 130.

[81] D. Akimov *et al.* (COHERENT Collaboration), COHERENT Collaboration data release from the first observation of coherent elastic neutrino-nucleus scattering, arXiv:1804.09459 [nucl-ex].

[82] D. Akimov *et al.* (COHERENT Collaboration), First constraint on coherent elastic neutrino-nucleus scattering in argon, Phys. Rev. D **100**, 115020 (2019).

[83] V. Belov *et al.*, The νGeN experiment at the Kalinin Nuclear Power Plant, JINST **10**, P12011 (2015).

[84] H. T. Wong, H.-B. Li, J. Li, Q. Yue, and Z.-Y. Zhou, Research program towards observation of neutrino-nucleus coherent scattering, J. Phys. Conf. Ser. **39**, 266 (2006).

[85] D. Y. Akimov *et al.* (RED-100 Collaboration), First ground-level laboratory test of the two-phase xenon emission detector RED-100, JINST **15**, P02020 (2020).